Montanuniversität Leoben

Processing and characterization of textured ceramic layered architectures

Masterarbeit am

Institut für Struktur- und Funktionskeramik

Montanuniversität Leoben

Anna-Katharina Hofer

Leoben, September 18

Affidativ

I declare in lieu of oath, that I wrote this thesis and performed the associated research myself, using only literature cited in this volume.

Eidesstattliche Erklärung

Ich erkläre an Eides statt, dass ich die vorliegende Diplomarbeit selbständig und ohne fremde Hilfe verfasst, andere als die angegebenen Quellen und Hilfsmittel nicht benutzt und die den benutzten Quellen wörtlich und inhaltlich entnommenen Stellen als solche erkenntlich gemacht habe.

Datum	Unterschrift

Danksagung

Ich bedanke mich bei dem Vorstand des Insituts für Struktur- und Funktionskeramik, o. Univ. Prof. Dr. Robert Danzer, für die Ermöglichung der Verfassung dieser Arbeit, und auch bei seinen Mitarbeiterinnen und Mitarbeitern, für deren Unterstützung und Freundlichkeit.

Weiters danke ich Gary L. Messing und dessen Team am Department of Materials Science and Engineering an der Penn State University, durch die es möglich war, einen Teil der Arbeit im Ausland durchzuführen.

Ein besonderer Dank geht an meinen Betreuer Dr. Raul Bermejo, für dessen bedingungslose Unterstützung. Ohne seine Mühen wäre die Arbeit in Amerika und die Fortsetzung in Leoben nicht möglich gewesen.

Ich danke der Material Center Leoben Forschungs GmbH für die Möglichkeit innerhalb eines COMET-Projektes mitzuarbeiten.

Der österreichischen Bundesregierung (insbesondere dem Bundesministerium für Verkehr, Innovation und Technologie und dem Bundesministerium für Wirtschaft, Familie und Jugend) vertreten durch die Österreichische Forschungsförderungsgesellschaft mbH (FFG), und den Ländern Steiermark und Tirol, vertreten durch die Steirische Wirtschaftsförderungsgesellschaft mbH (SFG) sowie die Standortagentur Tirol wird für die Förderung im Rahmen des COMET Förderprogramms herzlich gedankt.

Mein herzlicher Dank gilt der „Austrian Marshall Plan Foundation“ und der „European Ceramics Society“, durch deren finanzielle Unterstützung der Auslandsaufenthalt möglich war.

Ich möchte auch meinen Freunden und Studienkollegen danken, mit denen ich viel lachen kann, die mich beruhigen und mit denen ich Erlebnisse sammle. Besonderer Dank gilt auch meinem Freund, Tobias, der immer für mich da ist und viel Geduld beweist.

Mein größter Dank gilt meiner Familie, meiner Mama, Elisabeth, meinem Papa, Stefan und meinen Schwestern Sophia und Nuria, für die finanzielle und persönliche Unterstützung bei allem was ich mache.

Abstract

Ceramic materials are utilized for a wide variety of applications, as structural as well as functional components. Besides their outstanding mechanical, chemical and electrical properties, they have a very brittle character, which results in low fracture toughness, compared to e.g. metals. In addition, notwithstanding the high strength of ceramics, critical defects of different size introduced during processing, machining or in service yield a scatter in the failure stress of ceramic components that reduces their mechanical reliability.

The current design of ceramic materials in a “bio-inspired” layered architecture using either weak or strong interfaces, or with residual stresses has proved to be an effective barrier to the propagation of cracks from surface flaws, providing the material with a minimum design strength, and thus higher reliability. Recent work has demonstrated that tailoring the microstructure and architecture of such “bio-inspired” layered ceramics can significantly enhance their damage tolerance. A key is the combination of residual stresses and textured microstructure. The aim of this thesis was to investigate the combined effect of a tailored microstructure and architectural design to enhance the damage tolerance of alumina-zirconia based multilayer ceramics.

Several monolithic and multilayer samples were fabricated via tape casting, combining different microstructures (i) equiaxed and (ii) textured. The monolithic materials were characterized according to their microstructural, thermo-physical and mechanical properties. Material properties as the degree of texture, density, Vickers hardness, E-modulus, coefficient of thermal expansion and fracture toughness were determined. The layered architectures, classified in periodic and non-periodic, were fabricated with the corresponding embedded layers having the same or different thickness, respectively. The anisotropic thermal expansion coefficient in alumina (and tailored addition of zirconia) will yield thermal strain mismatch between textured and non-textured microstructures, and thus in-plane residual stresses. In the textured layers residual compressive stresses were induced. The residual stresses were aimed to be of a small magnitude so that no edge cracking would occur, but still effective for fracture toughness increase. The samples were tested via 4-Point-Bending, considering (i) natural and (ii) artificial flaws. The bending strength was determined in samples containing natural flaws and analyzed using Weibull statistics. Concerning the samples with artificial (indentation) flaws, effects such as crack arrest, crack deflection and crack bifurcation were observed and discussed.

Kurzfassung

Keramiken sind anorganische nichtmetallische Materialien, welche sowohl bei Struktur- als auch Funktionswerkstoffen zum Einsatz kommen. Sie beeindrucken durch herausragende mechanische (z.B. hohe Temperatur-, Oxidations- und Korrosionsbeständigkeit), chemische und elektrische Eigenschaften (z.B. stark nicht-linearer elektrischer Widerstand, hoher Piezo-elektrischer Koeffizient). Sie haben jedoch, im Vergleich zu metallischen Materialien, eine sehr geringe Bruchzähigkeit. Darüber hinaus führen Defekte unterschiedlicher Größe, eingebracht durch die Herstellung, die Bearbeitung oder während des Einsatzes, zu einer Streuung der Bruchspannung. Dies macht den Einsatz keramischer Bauteile in manchen Bereichen schwierig.

Um die Bruchzähigkeit von Keramiken zu verbessern, werden von der Biologie inspirierte Multischicht-Bauteile hergestellt. Die Grenzflächen zwischen den Schichten können schwach oder stark sein. In den Schichten können Eigenspannungen eingestellt werden. Beides kann eine effektive Behinderung der Rissausbreitung verursachen. Frühere Arbeiten haben gezeigt, dass durch die Texturierung des Gefüges und durch eine gezielte Architektur der Schichtdicke und -anordnung, eine deutliche Verbesserung der Bruchzähigkeit erreicht werden kann. Dabei spielt die Wechselwirkung der eingebrachten Eigenspannungen mit dem texturierten Gefüge eine wichtige Rolle. Ziel dieser Arbeit war es, den Effekt der Kombination aus Eigenspannungen, orientiertem Kristallgefüge und Designvarianten von Multischicht-Keramiken aus Aluminiumoxid-Zirkoniumoxid auf die Bruchzähigkeit zu untersuchen.

Es wurden einerseits monolithische Proben unterschiedlicher Kristallgefüge, (i) equiaxial und (ii) texturiert, und andererseits Multischicht-Proben (Laminate), welche eine Kombination aus den beiden genannten Strukturen darstellten, mittels Tape Casting hergestellt. Die mikroskopischen, thermisch-physikalischen und mechanischen Eigenschaften der monolithischen Materialen wurden gemessen. Der Grad der Kornorientierung (Textur), Dichte, Härte, E-Modul, thermischer Ausdehnungskoeffizient und Bruchzähigkeit wurden bestimmt. Bei den Laminaten wurde zwischen periodischen und nicht-periodischen Designs, bezogen auf die Dicke und Anordnung der verschiedenen Schichten unterschieden. Der anisotrope Wärmeausdehnungskoeffizient von Aluminiumoxid und die Dotierung mit Zirkoniumoxid verursachen verschiedene

thermische Dehnungen zwischen equiaxialen und texturierten Schichten. Dies wurde ausgenutzt um Eigenspannungen in den verschiedenen Schichten einzustellen.

In den texturierten Schichten sollten Druckeigenspannungen entstehen. Die Eigenspannungen sollten jedoch nicht zu groß sein, um "Edge Cracking" zu vermeiden, aber groß genug um die Bruchzähigkeit effektiv zu steigern. Die Proben wurden in 4-Punkt-Biegung geprüft, wo einerseits Proben mit (i) natürlichen und (ii) künstlichen Defekten untersucht wurden. Die Biegefestigkeit wurde an Proben mit natürlichen Defekten bestimmt, bzw. die Weibull-Verteilung der Festigkeit ermittelt. Bei den Proben mit künstlichen Defekten wurden Effekte wie Riss-Stopp, Riss-Ablenkung und Riss-Verzweigung beobachtet, bzw. analysiert.

Content

Acronyms and Abbreviations

a	Crack length	[m]
Al_2O_3	Aluminium oxide	
BB-Out	Binder-Burn-Out	
CIP	Cold Isostatic Pressing	
CTE (α)	Coefficient of Thermal Expansion	$[K^{-1}]$
E	Young's modulus	[GPa]
EA	Non-textured/equiaxed alumina	
HV	Vickers Hardness	[-]
TA	Textured alumina	
K_I	Stress intensity factor	$[MPam^{1/2}]$
K_{IC}	Fracture toughness	$[MPam^{1/2}]$
LF	Lotgering Factor	[-]
m	Weibull modulus	[-]
NP1	Non-periodic design 1	
NP2	Non-periodic design 2	
P	Periodic design	
TGG	Templated Grain Growth	
Y	Geometrical factor	[-]
ZrO_2	Zirconium oxide	
σ_0	Characteristic strength	[MPa]
$\sigma_{B,corr}$	Corrected bending strength	[MPa]
σ_{res}	Residual stress	[MPa]
_II	Parallel load	
_n	Perpendicular load	
3 / 4 PB	3- / 4-Point-Bending	

1. Introduction

1.1. Ceramics: properties and applications

The history of ceramics already started a long time ago, when humans used the inorganic material to form bricks, bowls or sculptures. These first applications of ceramic were made out of clay. With the exploration and fabrication of different materials the field of applications of ceramics expanded. Now, thousands of years later, the group of ceramic materials contains all the different inorganic non-metallic materials such as oxides, carbides and nitrides. The use of inorganic components has gained high importance in structural components and machine parts due to their outstanding mechanical properties such as high-temperature stability, oxidation and corrosion resistance, dimensional stability, hardness and wear resistance. Some examples are high temperature resistant parts for metallurgical processes, wear-resistant plates for paper machines, accurate position holders for optics, resistors and capacitors in microelectronic packages, piezo-ceramic controlled valves for engines, electrolytes in electrochemical solid oxide fuel cells and hard, bio-inert implants in medicine. Besides the good structural properties of ceramics, in comparison to other material groups as for example metals, they also show unique functional properties, e.g. extreme non-linear dependence of electrical resistance with temperature (used in thermistors), electric field (used in varistors) or a high piezo-electric coefficient (used in sensors and actuators). The stated properties make ceramics to a material of high importance for various different applications.

The structural behavior of ceramics is associated with the mechanical parameters such as elastic modulus (E), hardness (H), as well as compressive and tensile stress (σ). Ceramics show in general a linear elastic behavior with normally higher E-moduli than metals (e.g. Alumina: E = 250-400 GPa, steels: E = 180-250 GPa) [2]. This is due to the hybrid bonds, which are a mixture of ionic and covalent bonds, in ceramic materials, leading to a localization of the binding orbitals of electrons around the corresponding ion cores, which results in an immobility of the electrons. This immobility of the electrons is the reason why much more energy is needed to generate and move dislocations in ceramics, in comparison to metals. As a result, ceramic materials show in general elastic behavior, with almost no plastic deformation upon mechanical loading. Another important parameter for ceramics is the hardness, especially when high wear-resistance is required. The hardness of some alumina

materials can reach values up to 18 GPa, whereas it ranges from 1 to 2 GPa for mild steels and from 1.5 to 3 GPa for high-speed steels [3].

In terms of mechanical strength, ceramics can withstand large loads under compression (e.g. Roman bridges). However, in general, the tensile strength of ceramics is about 1/10 of their compressive strength. When tensile stresses are applied to ceramic materials, generally brittle fracture is observed without any plastic deformation. The brittle character of ceramic materials is one of the factors that limits the use of ceramics in some technical applications.

1.2. Colloidal processing: theoretical background

The so called "colloidal processing" was selected for this investigation. It is generally defined as the processing of ceramic powders in the colloidal size range, i.e. from 1 to 10^3 nm [4]. One of the advantages of using starting "colloids" is to achieve a better control of raw materials and processing conditions, thus limiting heterogeneities in the microstructure. This has enormous implications in the sintering step and thus in the properties of the final part. In the following, the importance of the stability of colloidal suspensions and the different sintering steps will be briefly described. A detailed information can be found in [4].

1.2.1. Stability of colloidal suspensions

In colloidal suspensions the powders experience repulsive and attractive (Van der Waals) forces when they are moving (kinetic energy). Depending on the particle size the repulsive forces increase with the third power of the particle diameter, whereas the Van der Waals forces increase linearly. As a consequence, for small particles the effect of the Van der Waals forces is much more dominant than the repulsive forces. The stability of colloidal suspension is very much related to the interaction between particles, and is usually described by the DLVO theory (Derjagin, Landau, Verwey and Overbeek), see Figure 1.

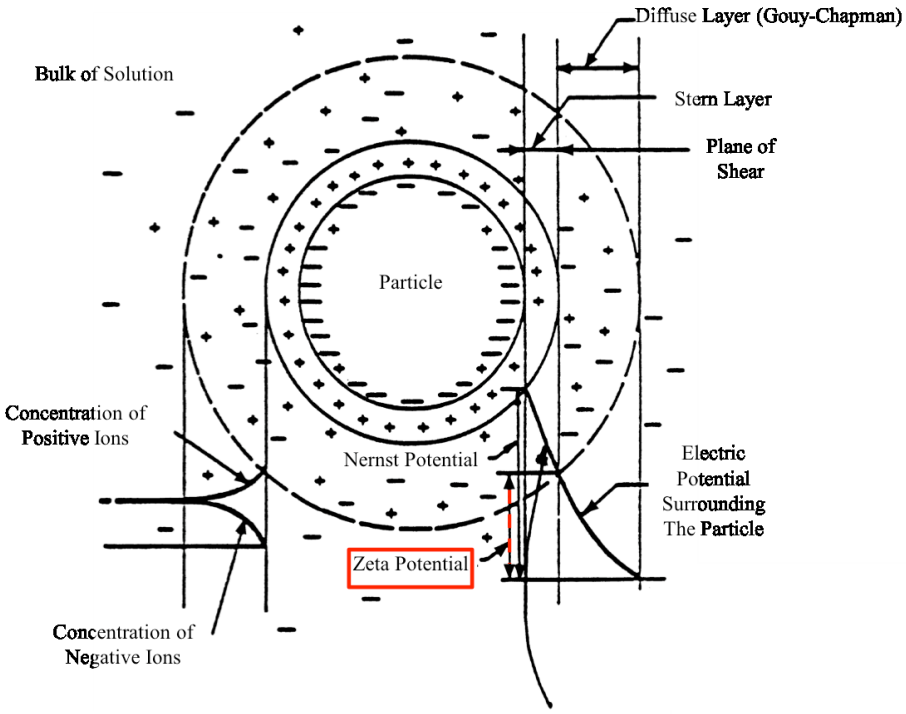

Figure 1. Double layer model after DLVO [1]

In the DLVO model the ionically charged surface of a particle is surrounded by a first layer of ions with opposite charge as the ions on the surface of the particle, called the Stern layer. Around this layer, the Diffuse layer (also called the Gouy-Chapman layer) is formed, containing negative as well as positive charged ions. The potential between these two layers, Stern and Diffuse layer, is the Zeta-Potential, which can be measured by moving either the particle or the liquid, in which the particles are dispersed. This movement causes a shift of the potential, which indicates the size of the ionic cloud. By measuring the Zeta-Potential, the right composition for a stable colloidal suspension can be defined [4,5]. Modifying the pH of the suspension will change its polarity, and thus the Zeta-Potential can be significantly varied between positive and negative (see Figure 2). The so-called Isoelectric Point (IEP) is defined as the pH at which the Zeta-Potential becomes zero. At this point the suspension is totally unstable, instantaneous “flocculation” occurs. To obtain a well dispersed stable suspension the pH should be at least four pH units either below or above the IEP, measured from the original pH of the material, see Figure 2. [1,5,6]

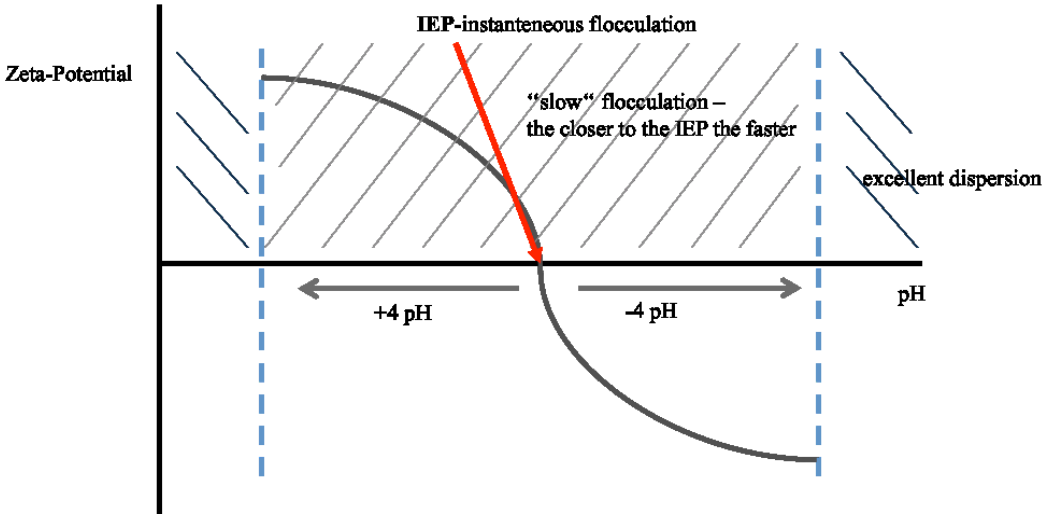

Figure 2. Schematic of a Zeta-Potential – pH curve showing stable and unstable regions of a dispersion

In general, for the fabrication of most ceramic materials a binder is needed in the forming process. Binders are polymers solved either in an aqueous or a non-aqueous liquid. It surrounds and holds the ceramic powder particles together via capillary forces. Adding a binder to the system allows handling the ceramic material before sintering without fracture (cracking). For the appropriate selection of the binder, the ceramic powder has to be "wettable" by the binder. This means a contact angle (θ) below 90° between the solid and the liquid surface, see Figure 3. This condition must be given to obtain well dispersed particles in the slurry.

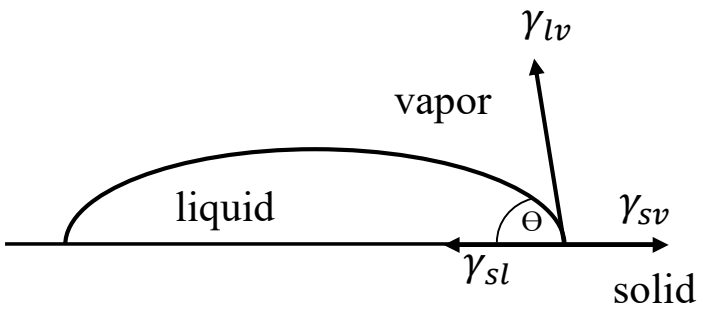

Figure 3. Schematic for describing the contact angle (θ), which should be <90° for good wettability

An important factor that has to be considered for the right selection of the binder system for the formulation of the ceramic slurry is the value of the pH from the binder as well as from the ceramic material. If the values of the two different components are more than about two

pH units apart, either flocculation or settling of the particles may occur at lower pH values, or if the pH gets too high, the alumina particles might start to dissolve. Flocculation is due to the change of the Zeta-Potential closer to the IEP of the ceramic material by adding a binder with a much different pH value. For instance, the pH value for alumina is 9.5, meaning the pH should not be higher than 11.5 or lower than 7.5 after adding the binder.

Besides the polymers of the binder, also other organic components are added, to achieve a better colloidal dispersion. Usually an additional dispersant is added, where the polymer-chains stabilize the particles, to avoid a direct contact between two particle surfaces. Another component which is commonly added is the plasticizer, which lowers the glass transition temperature of the polymer used as binder, to make it more flexible.

To ensure that the resulting slurry does not contain too much air a defoamer may also be added with the other components.

1.2.2. Sintering mechanisms

Beside the stability of colloidal suspensions, a very important step on the processing of ceramics is sintering, which can be described in three different stages: the Initial, the Intermediate, and the Final stage.

Initial stage: Here rearrangement of the particles occurs because of capillary forces, which results in an increase of the relative density (<75 %) due to the increase of contacts between the single particles. In the area where the particles touch each other necks are formed via diffusion of atoms from either the surface or the lattice of the ceramic particle.

Intermediate stage: Through diffusion material deposits more and more in the necks between the particles, resulting in a continuous pore channel network. Additionally, atoms diffuse from the neck towards the pores and reduce the amount of vacancies. In this stage a relative density of 75-92 % can be reached.

Final stage: Material that diffused towards the pore channels closes up the space and forms spherical pores. Due to the small size of the pores it is now easier for the grain boundaries to move. As a result, pores get isolated on triple points, shrink and are removed via diffusion. In this stage also grain growth occurs which is driven by the force of reducing the surface energy between two grains having different crystallographic orientations. Usually grain growth can be observed at relative densities from 92-95 %, where no interconnected pore network is still present. In the final stage a relative density of 100 % can be achieved. [7,8]

As mentioned in the three stages of sintering, diffusion is responsible for the reduction of the ratio of pores and the formation of a dense, continuous microstructure. During sintering several different mechanisms of diffusion can be observed, which can be divided in non-densifying and densifying mechanisms. The source for non-densifying mechanisms is the particle surface. From the surface of the particle the material diffuses either along the surface towards the contact between two particles (neck), or through the lattice or via vapor transport, see Table 1 and Figure 4. For the densifying mechanisms the source can either be the boundary between two particles as a result from the neck formation or dislocations in the particles. The diffusion of atoms from the boundary can occur via diffusion along the boundary on the one hand and via lattice diffusion on the other hand. In comparison to that, the diffusion of material from a dislocation in the particle can only be observed via the lattice, see Table 1 and Figure 4.

Table 1: Sintering mechanisms [7]

mechanism	Transport path	Source	Sink
	Non-Densifying		
1	Surface diffusion	Surface	Neck
2	Lattice diffusion	Surface	Neck
3	Vapor transport	Surface	Neck
	Densifying		
4	Boundary diffusion	Boundary	Neck
5	Lattice diffusion	Boundary	Neck
6	Lattice diffusion	dislocations	Neck

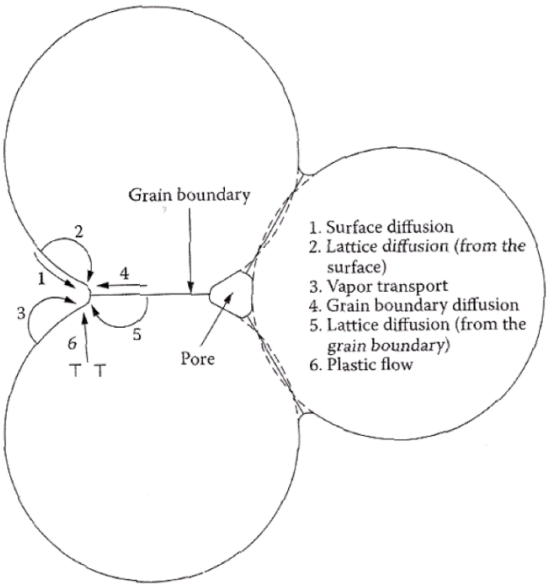

Figure 4. Schematic of the occurring diffusion mechanisms during sintering [7]

1.3. Brittle character of ceramics

Despite the outstanding properties of ceramics, there is a limitation for their use, due to their brittle character. In general ceramic materials show an elastic behavior when stress is applied following the Hook's law. The elastic modulus of e.g. alumina is 380-405 GPa, whereas steels show moduli between 180 and 250 GPa [3,9].

This brittle or elastic character of ceramics makes them very sensitive for any cracks or defects. These are located within the bulk and especially at the surface, resulting from the processing and/or machining procedures as well as from damage in service.

The influence of present cracks or defects in a ceramic microstructure can be described according to the Griffith and Irwin criterion, which describes the appearing stress intensity on a crack tip, depending on the applied stress and the crack length[3,10]:

$$K_I = \sigma \cdot Y \cdot \sqrt{\pi a} \qquad (1)$$

where K_I is the stress intensity factor in [MPam$^{1/2}$], σ is the applied stress in the (uncracked) sample in [MPa], Y is the non-dimensional geometrical factor of the crack and a is the crack length in [m].

There are three different opening modes for cracks (opening (I), sliding (II) and tearing (III)), depending on the direction in which the stress is applied. For ceramics the crack opening mode (I) has the most impact on crack propagation, therefore mainly the K_I is of interest.

It describes the needed stress σ that is necessary for the extension of a crack. If σ reaches a critical value, total failure occurs, resulting in a critical stress intensity factor (K_{IC}), which is known as fracture toughness.

The fracture toughness can be defined as the critical stress intensity factor at which a crack propagates instable in the material:

$$K_I \geq K_{IC} \quad (2)$$

K_{IC} for alumina is in the range of 3.0-4.0 MPam$^{1/2}$, whereas for steels it is 10 times higher, > 50 MPam$^{1/2}$ [3,10].

Due to the distribution of defects of different sizes within a ceramic material the strength varies from sample to sample, and from component to component. This leads to a statistically variable strength in ceramics, which can be described, in many cases, by the Weibull theory [11]. As a consequence of such behavior, there remains a (small) probability of failure even at very small applied loads (i.e. no lower bound for strength). Since flaws are intrinsic to processing and in most cases unavoidable, the mechanical strength and reliability of ceramic components is associated with the flaw distribution in the material. This scatter in strength affects the reliability and lifetime of ceramics, thus limiting the market potential and in some cases hindering the development of completely new markets for ceramic devices.

For the improvement of mechanical behaviors in ceramic materials various strategies have been adopted. Methods resulting in an increase of strength in ceramics have aimed to reducing the size of critical defects through, for example, colloidal processing, and/or the introduction of compressive residual stresses at the surface, as it is used for the strengthening in glass as in the Gorilla™ glass [12]. However, significant reduction of strength variability has not been achieved with these approaches.

In recent years, a “flaw-tolerant” concept has emerged for building tougher materials using a hierarchical structure as found in bone or nacre. The outstanding crack growth resistance of such natural systems is triggered in most cases by the combination of “intrinsic” and “extrinsic” toughening mechanisms acting at different length scales. As an example, the extraordinary toughness and strength of mollusc shells (see Figure 5) which is related to their fine-scale structure, namely a laminate of thin calcite crystallite layers consisting of 99 % calcium carbonate and tough biopolymers, arranged in an energy-absorbing hierarchical microstructure. The strength and toughness of such layered structures are significantly higher than those of their constituents [13]. In an attempt to improve engineering designs, textured

microstructures as well as architectural design have been aimed. Some examples can be found in the literature [14–16].

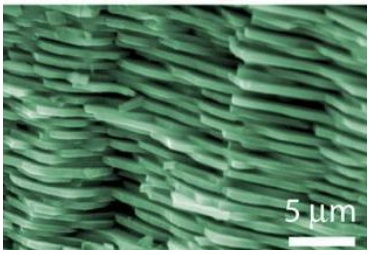

Figure 5. Step-wise fracture surface of a mollusc shell [13]

1.3.1. Textured microstructure

The fine-scale structure of a mollusc shell has been used as a model for the fabrication of crystallographic texture in ceramics, meaning a defined orientation of grains. Textured polycrystalline ceramics can achieve improved anisotropic properties comparable to single crystals. Tailoring the crystallographic orientation is of high interest when certain effects or properties improve, according to the textured grain structure. Applications, where the change of certain properties through anisotropy is utilized, are (i) magnetic ceramics, (ii) superconductors, (iii) ion conductors, (iv) thermoelectrics, (v) optical ceramics, (vi) thermal conductors as well as (vii) structural ceramics [14]. Depending on the application and the material, different techniques have been developed for the fabrication of a crystallographic structure. There are four general techniques, with which texture fractions of >90 %vol can be achieved. These include (i) the Rolling Assisted Biaxially Textured Substrates process (RABiTS) [17], (ii) the powder-in-tube (PIT) [18], (iii) the templated grain growth (TGG) and the reaction templated grain growth (RTGG) [19,20], and (iv) the strong (7-14 T) magnetic field alignment (MA) of particles [21]. Among these techniques, TGG has been extensively utilized in alumina-based materials to obtain high degree of texture, and will be explained in more detail in the following.

Templated grain growth (TGG) is a process that occurs during the sintering stage. To induce TGG several previous processing steps have to be accomplished. First, a colloidal suspension, consisting of (i) powder particles of a certain material (e.g. alumina), (ii) templates of the same material, which are bigger than the powder particles and having a flake-like shape, (iii) components for liquid phase sintering and (iv) a binder system are mixed together. For achieving a textured microstructure after sintering the templates have to be

aligned already in the suspension. The alignment of the templates can be obtained using the tape-casting method [14,22]. The orientation of the templates is influenced by the magnitude of torque and shear stress during casting, the ratio of casting height and template diameter. After the aligning of the templates, further processing steps such as uniaxial pressing, hot isostatic pressing and binder burn out are carried out; however, these steps will not influence the resulting textured orientation of the grains. Finally, sintering is performed at high temperature, the microstructure evolution is dependent upon the aligned templates. A solution-precipitation process takes place, where the smaller particles are able to "dissolve" and then "precipitate" onto the bigger particles (templates), thus adopting a preferential orientation. The phenomenon that the big particles (templates) grow on the small ones can be described with the Oswald ripening [23]. This effect occurs due to driving force of minimizing the surface energy of the system. The surface tension of big particles is comparably low to small particles. As a result the solubility of small particles increases, leading to their dissolution and precipitation onto the big particles, and the growth of the templates, see Figure 6 [14] The present liquid phase, which may be enhanced by the addition of certain components to the colloidal suspension, facilitates the transport of material and foster abnormal grain growth.

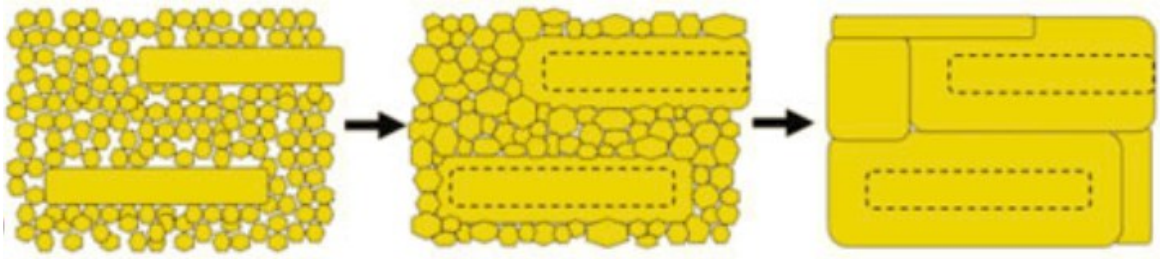

Figure 6. Stages of templated grain growth during sintering [14]. Big particles grow at the expense of the smaller particles.

Using this method a large volume fraction of oriented grains in the microstructure (so-called "degree of texture"), over 90 %vol can be achieved [24]. With a degree of > 90 %vol textured structure in polycrystalline materials, functional properties comparable to those of a single crystal can be obtained.

In terms of mechanical properties, textured materials have shown improvement of certain properties such as hardness and/or toughness, due to the anisotropic grain orientation and morphology [14]. Considering the hardness for example, hexagonal single crystal as alumina show a higher Vickers hardness perpendicular to the (0001) surface (HV=23.0 GPa) [25]. In

comparison textured alumina shows a hardness of 16.5 GPa, and non-textured alumina 16 GPa according to Carisey et al [26].

The increased hardness in the (0001) direction also affects the improvement of fracture toughness by making it more likely for cracks to propagate through grains and deflect parallel to the basal surface rather than perpendicular to it. Additionally, the morphology of the grains may induce phenomena such as grain bridging, interfacial bonding and energy dissipating mechanisms appearing during crack propagation, resulting in an increase of fracture toughness. Pavlacka and Messing reported an effective fracture toughness (measured using the indentation-strength method) of ~4.6 $MPam^{1/2}$ when measuring parallel to the basal surface of [0001], compared to ~2.6 $MPam^{1/2}$ measured perpendicular to the basal surface [22].

Another beneficial effect of a textured microstructure is the reduction of residual stresses in the sintered part, reducing the probability of microcracks formation. It is known that the coefficient of thermal expansion is different according to the different directions of a crystal. As a result, in textured microstructures the expansion is organized in the parallel and perpendicular direction, leading to lower residual stresses than in equiaxed structures [27].
All the described effects, resulting from the textured orientation of the grains make it possible to improve the mechanical properties of structural ceramics [14].

1.3.2. Layered composites of different materials

Nowadays, for next generation devices it is necessary to combine materials (ceramic, metals and polymers) that can bring new functionality to components. The fabrication of such laminates is enabled through the technique of tape casting. Combining different materials with their certain beneficial properties might be an interesting thought, though it can be a challenge from the structural viewpoint. The different coefficients of thermal expansion (*CTE*) and elastic properties of the combined materials can generate significant “residual stresses” in some of the parts. While tensile residual stresses may lead to the initiation and/or propagation of cracks from starting defects, even before service loading conditions, compressive residual stresses can be beneficial in strengthening the material. As a consequence of a residual stress distribution in the layered composites, the resistance of the material to the propagation of an existing crack depends on the location within the layered architecture. This means that the (apparent) fracture toughness of the multilayer, $K_R(a)$, depends on the crack length, a. An

estimation of $K_R(a)$ can be attained using the "weight function" approach or using numerical methods (more details in [4]), according to:

$$K_R(a) = K_{Ic} - \int_0^a h(a,x) \times \sigma_{res} dx \quad (3)$$

where $K_R(a)$ is the apparent fracture toughness as a function of the crack length (a), $h(a,x)$ is the so-called weight function (taking into account the geometry of the sample and crack and loading configuration), σ_{res} is the in-plane compressive/tensile residual stress in the corresponding layer and K_{IC} is the critical stress intensity factor (fracture toughness) of the corresponding layer where the crack tip is located [28].

Models based on fracture mechanics analyses have been attempted in the literature in order to rationalize the crack propagation behavior in heterogeneous structures. Figure 7 shows an example to model the change in apparent fracture toughness, $K_R(a)$ of a layered material, influenced by the tensile or compressive residual stresses in the different layers. It is shown how K_R first decreases when the crack propagates through the outer most (tensile) layer (blue thick tensile layer in Figure 7. When the crack reaches the interface of the two different materials, K_R increases remarkably (yellow thin compressive layer in Figure 7). The consequence of having an internal compressive layer is that the propagation of the crack may stop, if the apparent fracture toughness within the layer, $K_R(a)$, is greater than the applied stress intensity factor, $K_{appl}(a)$, as given by Eq.(1) (see more details on the model in Refs. [15,29]).

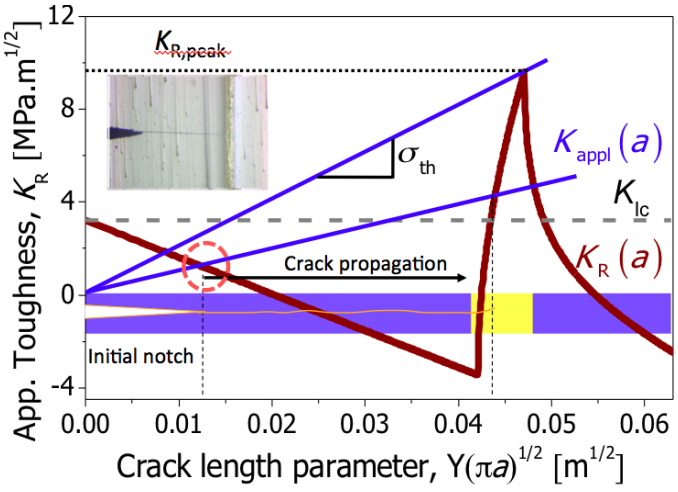

Figure 7. Model of the apparent fracture toughness in a multilayer compound [15]

Recent investigations based on fracture mechanics analyses have shown huge potential for a significant increase of the mechanical properties (i.e. toughness and threshold strength, defined as a "minimum strength" for the material) of layered systems by tailoring the residual stresses in a symmetric and non-periodic[δ] multilayer architecture (see Figure 8) [30]. The referred figure shows the "apparent" fracture toughness of a periodic (P) and a non-periodic (NP) laminate, having the same magnitude of tensile (light yellow layers) and compressive (dark blue layers) residual stresses, respectively. The slope of the lines gives the threshold (lower bound) strength, σ_{th}, of the system. The non-periodic architecture shows higher toughness and higher threshold strength (see Ref. [30] for more details). The consequence of this prediction with respect to periodic laminates is that one can improve the threshold strength and toughness of the system using the same residual stresses as available in the periodic design. This approach would provide ceramic components with significantly higher mechanical properties and reliability.

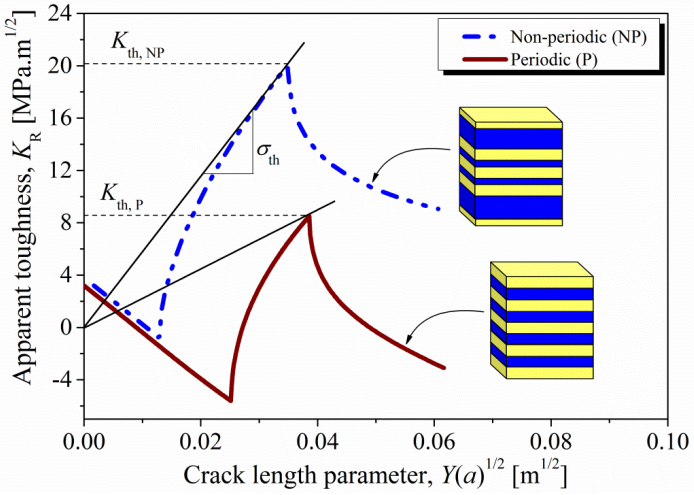

Figure 8. Apparent toughness of a non-periodic (NP) and periodic (P) laminate, with the same tensile and compressive residual stresses in the layers. The slope of the lines gives the threshold strength, σ_{th}, of the laminate. The non-periodic architecture shows higher toughness, K_{th}, and threshold strength [28].

Besides the potential of using residual stresses for crack arrest and the additional effect of non-periodic distribution of layers, crack deflection is a further effect, appearing in layered composites, that may increase the fracture toughness of the material (see some examples in

[δ] The term "*non-periodic*" refers to layered architectures where the layers of a certain material may not have the same thickness through the laminate (*e.g.* a sequence such as A**BB**A**B**A**BB**A).

Refs. [4,15,29]). In general, for non-textured polycrystalline ceramics, cracks usually propagate perpendicular (transverse) to the applied stress. However, in textured microstructures crack deflection may occur, which can be described after the model of He and Hutchinson, considering the interface of two adjacent platelets [31]. Whether a crack penetrates or deflects depends on the ratio of the critical energy release rate of the potential deflected crack (G_d) to the critical energy release rate of the potential penetrating (transverse) crack (G_p). This ratio defines the regions, where crack penetration or crack deflection occurs, as seen in Figure 9.

Since the platelets are of the same material, no elastic mismatch is expected. As a result, crack deflection occurs if the interfacial fracture resistance, Γ_i, is less than 25 % of the fracture resistance, G_c ($\Gamma_i/G_c \leq 0.25$).

Furthermore, the presence of compressive stresses in the textured layers may enhance the deflection of cracks. The function delimiting crack deflection versus crack penetration, i.e. G_d/G_c, may be shifted due to the presence of compressive residual stresses in the textured layers. This can be described with a non-dimensional length parameter (η_{res}) for multilayer systems as followed:

$$\eta_{res} = \frac{\sigma_{res} \cdot a_p^{\lambda}}{k_I} \tag{4}$$

where σ_{res} is the compressive residual stress of the textured layer in [MPa], a_p is the flaw size at the interface of the platelets in [m], λ is a stress singularity exponent and k_I is a factor proportional to the applied stress field. Taking into account the compressive residual stresses, with a negative sign, values smaller than zero are achieved for η_{res}, resulting in an upward shift of the G_d/G_c curve. As a consequence, the region of crack deflection extends, and deflection may already occur at a bigger ratio of Γ_i/G_c (i.e. relatively strong interfaces). More details on the crack-deflection model in laminates can be found in Ref. [15,29].

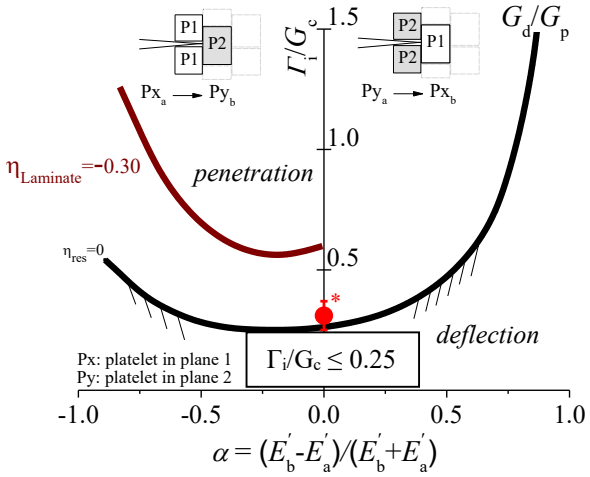

Figure 9. Model for assessing the crack penetration or deflection between two adjacent platelets based on He and Hutchinson plots [31]

2. Aim of the work

The aim of this work is to fabricate and characterize multilayer ceramic architectures designed with embedded layers having in-plane compressive residual stresses and a textured microstructure. The novelty of this work is to tailor the location of the textured, compressive layers in a “non-periodic” architecture. Though, the magnitude of the residual stresses shall be of a magnitude that is too small to cause edge cracking, but big enough to promote effects as crack arrest, deflection and bifurcation.

It is hypothesized that the combination of a tailored (textured) microstructure and architectural design (non-periodic laminate) will significantly enhance the damage tolerance of alumina-based multilayer ceramics.

3. Experimental Work

In this section the different materials for the fabrication of non-textured (equiaxed) and textured microstructures, as well as the layered architectures will be described. Special attention will be given to the processing of the materials and architectures, including all the different steps from slurry preparation, through tape casting, to sintering. As final step in the experimental work, the characterization of the fabricated samples will be described, according to their microstructural, thermo-physical and mechanical properties.

3.1. Materials of study and architectures

There is a wide variety of advanced ceramics for structural applications, which can be classified in oxide and non-oxide systems. The formers are for example Aluminium oxide (=Alumina, Al_2O_3), Zirconium dioxide (=Zirconia, ZrO_2), Magnesium oxide (Magnesia, MgO) or Titan(IV)-oxide (Titania, TiO_2). These inorganic compounds mainly consist of ionic bonds. Non-oxide ceramics are for instance Silicon nitride (Si_3N_4), Silicon carbide (SiC) or Aluminium nitride (AlN), holding more covalent bonds rather than ionic bonds, which results in much higher bond energies than for oxide ceramics [10]. Among the different ceramics, alumina and alumina-zirconia composites (i.e. a combination of both materials) were selected for this study.

For technical ceramic applications alumina is employed to 80 %. It is extracted from Bauxite via the Bayer-Process and can exist as different phases (e.g. γ (cubic), θ (monoclinic)). The most common is the α-phase, also called corundum, which has a rhombohedral crystal structure. This structure is built through large oxygen ions (anions), showing a formation of a hexagonal close packed array. Two thirds (for charge neutrality maintenance) of the octahedral sites of this hexagonal array are filled with Aluminium ions (cations) (see Figure 10) [32].

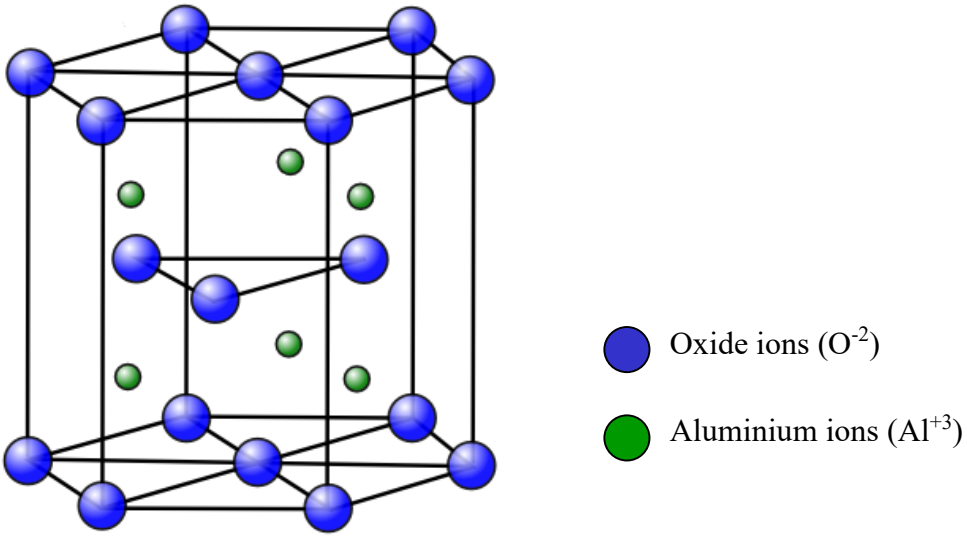

Figure 10. Crystal structure of Aluminium oxide (Al_2O_3) [33]

Zirconia actually occurs in a monoclinic crystal structure at room temperature. At a temperature of about 1170 °C it transforms into a tetragonal phase and at ~2370 °C into a cubic phase. Due to the martensitic transformation from the cubic phase to the tetragonal, higher toughness than in the monoclinic phase can be achieved. However, the temperature at which tetragonal zirconia is stable is ~1170 °C, therefore Yttriumoxide (Y_2O_3) is used to stabilize this phase at room temperature. Yttrium ions occupy positions of Zr^{4+} ions and as a result induce vacancies of oxygen (see Figure 11). [34]

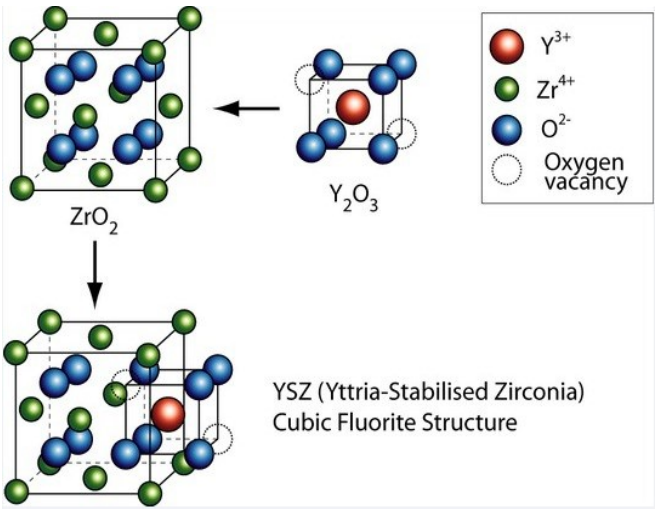

Figure 11. Process of doping ZrO_2 with Y_2O_3 to stabilize the tetragonal phase [35]

3.1.1. Monolithic materials

Monolithic samples consisting of one or two phases were fabricated to determine thermo-physical and mechanical properties of the main materials: (i) non-textured (equiaxed) alumina (with 5 %vol tetragonal zirconia) and (ii) textured alumina.

3.1.1.1. Equiaxed (non-textured) Alumina

Non-textured alumina shows an equiaxed microstructure, meaning that the grains do not show any preferential orientation. In the equiaxed material it was required to have small grain sizes, due to the improvement of mechanical properties and the result of a better interface between non-textured and textured materials for the layered architectures. To prevent grain growth in alumina, it was doped with 5 %vol of yttrium stabilized zirconia. This second phase causes the so called “pinning effect”, where the movement of alumina grain boundaries is inhibited due to the small zirconia particles [35,36]. Moreover, since zirconia has a larger coefficient of thermal expansion (*CTE*) ($\alpha(ZrO_2)$ = 10E-6 K^{-1}) [34], the addition to the alumina ($\alpha(Al_2O_3)$ = 5.43E-6 K^{-1}) [32] will increase the *CTE* of the non-textured alumina composite (as investigated in previous work [15])**,** thus introducing residual stresses during cooling from the sintering step. All the dimensions of the sintered and green stage specimens are listed in Table 2.

3.1.1.2. Textured Alumina

Textured materials can be fabricated using different techniques, for example uniaxial pressing during the sintering process or for metallic materials applying a magnetic field for particle orientation. In this study Templated Grain Growth (TGG) was applied to achieve a high degree of orientation of the alumina grains [19]. Here 95 %vol. of the solids was alumina powder (particle size ~ 0.20 µm) and 5 %vol. alumina templates, which are platelets having a flake like shape (diameter ~3 µm, thickness ~ 0.10 µm). [15]

See Table 2 for the desired sintered dimensions and the corresponding green part dimensions.

3.1.2. Layered architectures

For the layered architectures, textured (TA) and non-textured (EA) materials were combined in different designs. To compare the effect of different thicknesses in the samples on the mechanical properties (especially the effect of outer layers), three designs were fabricated. It must be highlighted that the volume ratio between the textured (V_{TA}) and non-textured (V_{EA}) materials was fixed to $V_{TA}/V_{EA} = 1/6$ for all designs. This volume ratio was selected based on previous studies on alumina-zirconia periodic laminates, showing the benefit of a relatively large volume ratio between the materials employed in terms of residual stress distribution and correspondingly mechanical behavior.

Two different layered systems in terms of layer distribution were designed and fabricated: a periodic (P) architecture and a non-periodic (NP) architecture.

- The periodic samples (P) consisted of 9 layers in total, alternating non-textured and textured material, where non-textured (equiaxed) material formed the outer most layers. The sequence was: EA-TA-EA-TA-EA-TA-EA-TA-EA.
- The non-periodic samples were built alternating 5 layers, where the outer equiaxed layer had a much lower thickness compared to the embedded (textured) layer. The middle layer showed a very high thickness, to fulfill the volume ratio of 1:6. For the non-periodic design two different architectures were fabricated (referred to as NP1 and NP2), differing in the thicknesses of the outer most and second layer. The sequence was EA-TA-EA-TA-EA.

Figure 12 shows the periodic design (Figure 12a) and the two non-periodic architectures (Figure 12b) and c)). The layers colored in blue, display the non-textured material, where the white arrows indicate the presence of in-plane (i.e. parallel to the layer plane) residual tensile stresses, occurring due to the different thermal expansion of the various materials. In contrast, the yellow colored layers, illustrating the textured material, show residual compressive stresses, indicated by the red arrows.

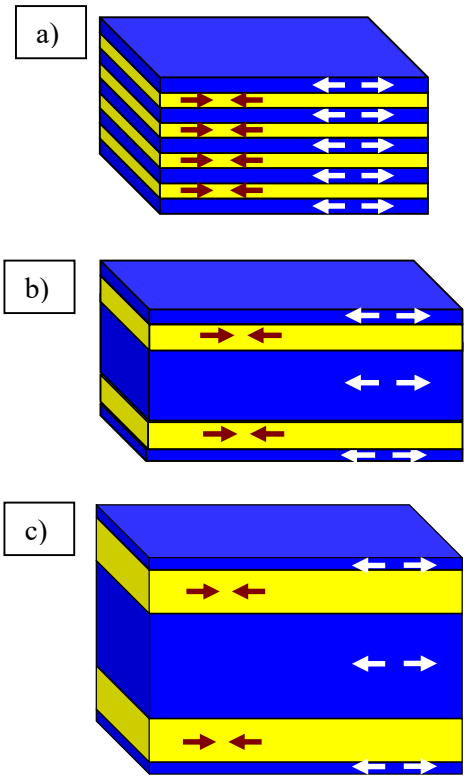

Figure 12. Schematic of **a)** Periodic design (9 layers), **b)** non-periodic design 1 and **c)** non-periodic design 2 (5 layers)

In Table 2 all the desired dimensions of the final sintered samples and the dimensions of the green parts are given, calculated considering the shrinkage of the monolithic samples.

Table 2: dimensions of monolithic and laminated samples in the green stage and the sintered stage, considering the shrinkage during processing[1]

			green dimensions	desired dimensions (after sintering)	shrinkage
			[µm]	[µm]	[%]
Equiaxed Alumina (EA)	layer	1	3710	3000	-19.19
Textured Alumina (TA)	layer	1	3860	3000	-22.35
Periodic (P)	layer	1	485	360	-25.77
		2	90	75	-16.67
		3	485	360	-25.77
		4	90	75	-16.67
		5	485	360	-25.77
		6	90	75	-16.67
		7	485	360	-25.77
		8	90	75	-16.67
		9	485	360	-25.77
Non-Periodic: design 1 (NP1)	layer	1	80	50	-37.50
		2	200	150	-25.00
		3	2240	1700	-24.11
		4	200	150	-25.00
		5	80	50	-37.50
Non-Periodic: design 2 (NP2)	layer	1	80	50	-37.50
		2	333	250	-25.00
		3	3800	2900	-23.68
		4	333	250	-25.00
		5	80	50	-37.50

[1]all the data are **estimated values**; due to the different materials, thermal expansion of these and different thicknesses in NP, the shrinkage in the laminates can not only be predicted by considering the shrinkage of the monolithic parts;

3.2. Processing of monoliths and laminates

In a first step, monolithic samples (textured and non-textured) were fabricated to be used as reference materials. Special effort was put on the optimization of the so-called templated grain growth (TGG) process to *texture* the materials under consideration [19]. In a second step, layered architectures combining textured and non-textured "tapes" were fabricated. In this regard, two different configurations were fabricated: (a) periodic and (b) non-periodic, referring to the distribution of the "embedded" layers within the multilayer structure (see section 3.1 for more details).

For the fabrication of the monolithic and laminated samples, tape casting was chosen as the processing route. The tape casting process, as conducted in this investigation, covered the following main steps: (i) selection of powders and binder system, (ii) preparation of the slurries, (iii) casting of slurries, (iv) hot pressing and lamination, (v) binder burn-out, (vi) cold isostatic pressing, and (vii) sintering.

3.2.1. Selection of powders

For the fabrication of the monolithic (textured and non-textured) and the layered samples three kinds of powder were applied. The main powder, which formed the matrix of all the fabricated samples, was the α-Alumina powder (AKP-50, Sumitomo Chemicals, Tokyo, Japan). This powder has a D_v50 (50 % of particles have a particle size below this dimension) is 0.204 µm, and a range of particle sizes from 0.086 µm to 0.345 µm. For the textured samples templates were added to obtain templated grain growth. These α-Al_2O_3 templates (Rona Flair® White Sapphire, EMD Performance Materials Corp., Darmstadt, Deutschland) had a thickness of ~0.10 µm and a diameter of ~3 µm. The third powder was only applied to the non-textured material, Yttria-stabilized zirconia powder (TZ-3Y, Tosoh, Tokyo, Japan) with a particle size of 0.60 µm.

3.2.2. Binder System

In this study an Acrylic binder system was applied to the ceramic powder. This binder system contained a water based binder (WB4101), a plasticizer (PL008), a dispersant (DS001), and a defoamer (DF002) (Polymer Innovations Inc., Vista, CA, USA).

3.2.3. Preparation of the slurry

In the following two different preparation procedures for the slurries will be described. First the preparation of the slurry for textured samples using the Acrylic binder system and then the preparation of the slurry for equiaxed samples with the Acrylic binder system and zirconia as dopant will be described.

To obtain templated grain growth and as a result a textured structure, a liquid phase has to be present during the sintering process. Therefore, the dopants CaO ($Ca(NO_3)_2$, BDH Chemicals, Radnor, PA, USA) and SiO_2 (Aerosil 200) are added to the slurries for textured samples, which form the liquid phase during sintering. The ratio of CaO : SiO_2 = 1 : 1, and the experimentally analyzed ideal amount of these dopants is 0.25 wt% of the total amount of ceramic material. Here CaO was added in form of $Ca(NO_3)_2{*}4H_2O$ after dissolving it in 5 ml of DI-H_2O [15].

a) Preparation of the slurry with the Acrylic binder system for textured samples:

Due to the formulation as listed in Table 3a) the Acrylic binder components were mixed together in a beaker and stirred on a stir plate. After 30 minutes the dopants $Ca(NO_3)_2{*}4H_2O$ and SiO_2 were added and mixed with the binder system for 1 h. Following, the alumina powder was weighted into the ball mill bottle, as in a) this bottle was filled to 1/3 with 5 mm in diameter Al_2O_3 beads, and additionally the stirred binder and dopants were added.

This slurry was mixed on the ball mill for 24 h, then after adding the Al_2O_3 platelets another 30 minutes. After milling, the slurry was sieved in a beaker and stirred for at least 24 h to remove the trapped air. The beaker with the slurry was put in a vacuum executor for 10 min and on a vibratory table for about 5 minutes to ensure that the slurry is totally air-free.

b) Preparation of the slurry with the Acrylic binder system and Zirconia for non-textured samples:

As described in a) the organic components of the Acrylic binder system (see Table 3b)) were stirred in a beaker for 30 min first. For non-textured samples no liquid-phase is necessary during the sintering process, therefore no dopants had to be added in this preparation. The binder system and the ceramic powders, alumina and zirconia, were then mixed together in the ball mill bottle and milled for 24 h. After milling and sieving the

slurry into a beaker the slurry was stirred for 24 h, as already explained in a) to remove the trapped air. To ensure an air-free slurry, it was put into the vacuum executor for 10 min and on the vibratory table for 5 min.

Table 3: Formulation of slurries for textured and non-textured samples

a) Slurry with Acrylic binder for textured samples

Alumina powder	82.5034 vol%	Acrylic binder	
Acrylic binder solution	13.0158 vol%	DI-H_2O	48.98 vol%
		WB4101	43.90 vol%
		PL008	3.91 vol%
		DS001	2.55 vol%
		DF002	0.66 vol%
$Ca(NO_3)_2$ *$4H_2O$	0.1108 vol%		
SiO_2	0.0281 vol%		
Al_2O_3 platelets	4.3419 vol%		

b) Slurry with Acrylic binder for non-textured samples

Alumina powder	76.87 vol%	Acrylic binder	
Acrylic binder solution	14.84 vol%	DI-H_2O	54.31 vol%
		WB4101	41.33 vol%
		PL008	3.74 vol%
		DF002	0.62 vol%
Zirconia	8.29 vol%		

3.2.4. Tape Casting

Tape Casting of ceramic materials is a forming process to fabricate tapes with thicknesses between 25 µm and 1000 µm [37]. The operating mode of tape casting is that the slurry is poured into a fixed doctor blade. This doctor blade is put on a polymer foil, which is pulled from one side of the machine to the other. Between the foil and the blade there is a gap, through which the slurry can run on the foil while it is pulled, see Figure 13.

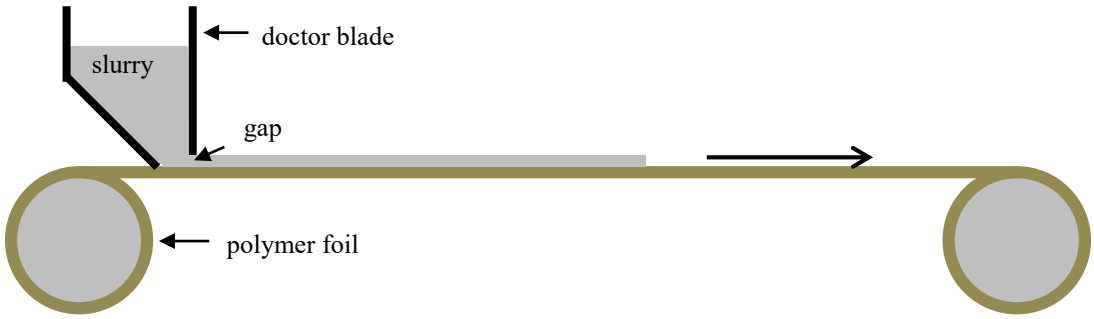

Figure 13. Scheme of the tape casting forming process

For achieving the desired thickness of the tape and the preferred orientation of the templates in the textured material through torque depending on the gap height and velocity of the polymer foil, adjustments had to be made on the tape casting machine.
The gap-height was 254 µm, which was adjusted manually with a metallic lamella that had the required thickness.

The foil that was used for tape casting was a mylar (polymer sheet) material, which had one non-coated side and one side coated with Silicon. For the tape casting of the alumina slurry the non-coated side was used. Otherwise, the effect of non-wetting would have occurred and an incoherent tape would have resulted, see Figure 14a).
After filling the doctor blade with the slurry the tape caster was run with a constant speed of 20 % of the motor speed (i.e. ~50 cm/min). The selection of the motor speed, depends on the viscosity of the slurry; the higher the viscosity the higher the velocity of pulling the mylar.

The casted tape was then dried in air for 24 h, before moving forward to the next processing step.

Cutting:
The next step of the fabrication process was to cut the tape, which had a length of about 1.50 m, a width of 110 mm and a thickness of 60-75µm. The thickness variation depended on the viscosity of the slurry. The final dimensions of the tapes were ~50x50 mm. Those cut layers were then stacked according to the required architecture and sample thickness that were to be fabricated.

Figure 14b) shows a dry tape, cut into the right dimensions.

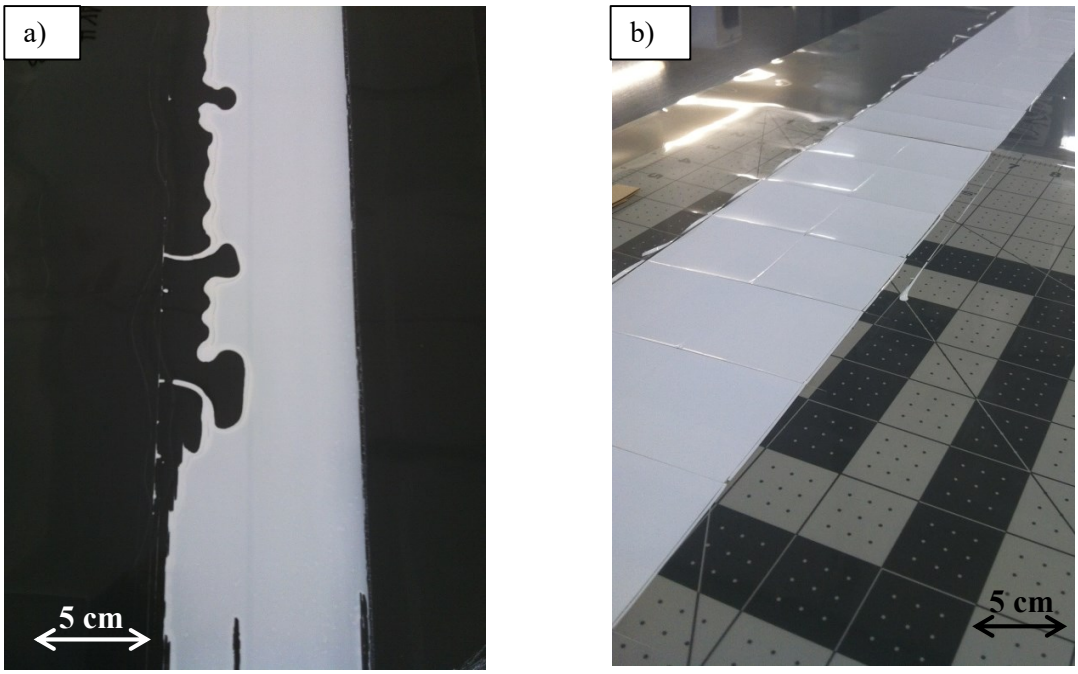

Figure 14. a) shows a non-wetted tape; **b)** a well wetted tape on the non-silicon coated side cut into the required dimensions is seen

3.2.5. Hot Pressing (HP) & Lamination (IP)

The next processing step is the hot pressing (HP) of the stacked layers, where the last layer on each side were kept as mylar material for the protection of the sample during pressing. The sample was put between two metallic tiles and hot pressed at a temperature of 75 °C at a pressure of 2 tons for 15 min.

After hot pressing, one of the metallic tiles was removed and a fitting rubber piece was put on top of the sample. This was then laminated and isostatically pressed at 75 °C (IP), with a pressure of 20 MPa for 30 minutes.

These processing steps (HP&IP) were performed to obtain a compact sample and remove some porosity between the stacked layers.

3.2.6. Binder Burn Out (BB-Out)

As mentioned above, the binder was added earlier to obtain a slurry with a viscosity, appropriate to cast the tapes and to give a certain strength and flexibility to the tape to be able to handle it without fracture. However, after the green state, the binder has to be removed (if possible to 100%). It is important that the binder is totally removed from the part, otherwise the organic components might get trapped in the ceramic structure due to the change of an open pore to a closed pore structure during sintering and, as a

consequence, the evaporation of the polymer phase could cause cracking during sintering at higher temperatures. The process for the removal of the organic components was divided into several steps with different temperatures and dwelling times (see Figure 15), as follows:

First, after setting the ceramic sample on a porous ceramic holder into the furnace, the part was heated with a rate of 0.2 °C/min to a temperature of 350 °C, where it was dwelled for 9 h. In this step the plasticizer is removed, which has the lowest boiling temperature of the organic components. In a second step, the temperature was increased to 450 °C also with a rate of 0.2 °C/min and held for 4 h. At 450 °C all the other polymers were evaporated so that only an open pore ceramic structure was left. Following, the furnace was cooled down to room temperature with a rate of 1.6 °C/min.

After binder burn out, the sample was very brittle, therefore caution had to be taken at handling the material

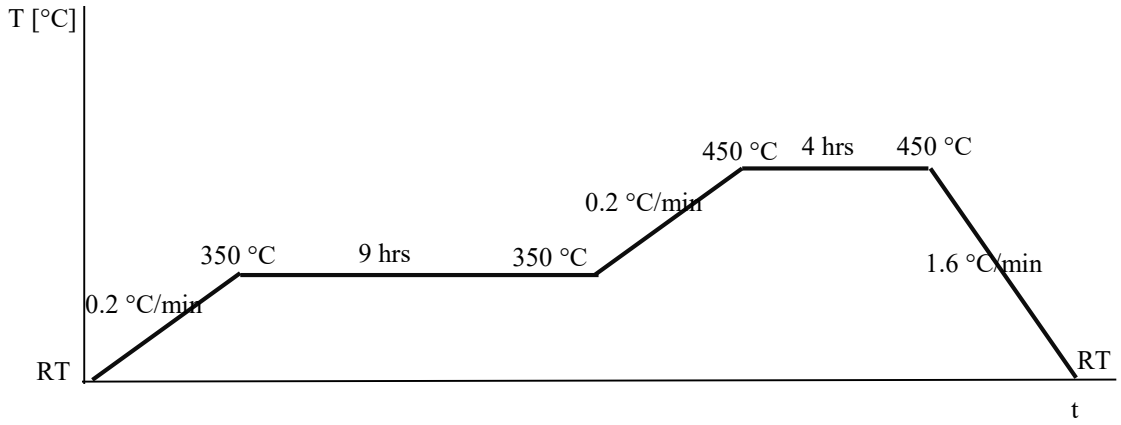

Figure 15. Diagram of the Binder Burn Out process for the Acrylic binder system

3.2.7. Cold Isostatic Pressing (CIP)

Cold isostatic pressing (CIP) was applied to compress the ceramic sample after binder burn out in order to achieve a high density (~99%) after sintering. For the CIP the sample was vacuum sealed in two latex gloves and then cold isostatically pressed at 200 MPa.

3.2.8. Sintering

The sintering of all the samples was carried out in a high temperature furnace at a temperature of 1550 °C. For the final processing step the part was placed on a crucible

covered with tabular alumina and put into the furnace. This was heated with a rate of 5 °C/min up to 1550 °C and dwelled for 4 h, see Figure 16.

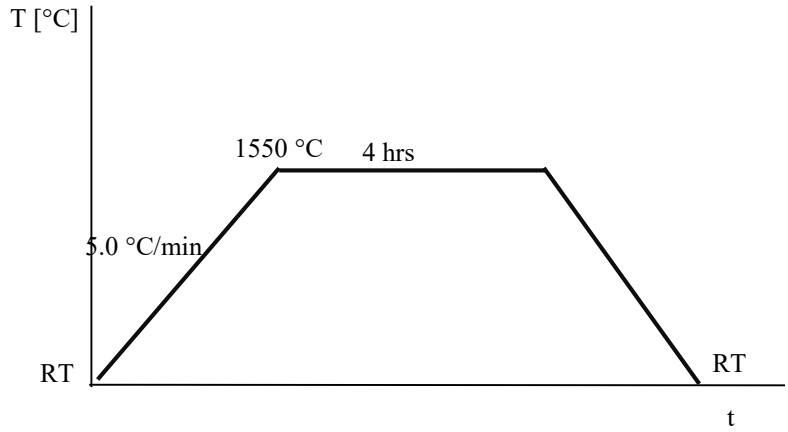

Figure 16. Diagram of the sintering process

3.3. Microstructural and Mechanical Characterization

3.3.1. Sample Preparation

The final sintered samples fabricated using tape casting had the dimensions of about 40x40x3 mm. For microstructural and mechanical characterization, the sintered plates were cut into prismatic bend bars with dimensions of about 40x3x3 mm. These specimens were accordingly prepared, depending on the type of characterization.

3.3.1.1. Grinding and Polishing

All specimens were grinded and polished on the surface perpendicular to the layers, independently for which kind of characterization a specimen was used (see Figure 17).

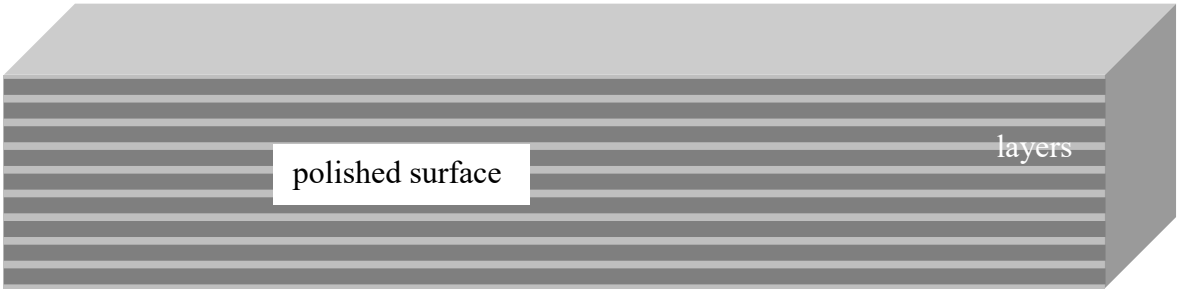

Figure 17. Orientation of the layers according to the polished surface

For this preparation the samples were glued on a circular plate using wax. The plate was then fixed on a grinding machine, using a Struers Pedemax-2 (Struers Tech, DK2610 Copenhagen, Denmark). The following grinding and polishing steps were carried out with different grades of the discs grid, see Table 4.

Table 4: Steps of grinding and polishing

step	Grid grade	Time
	[µm]	[min]
1	20	5
2	9	10
3	6	10
4	3	10
5	1	10

3.3.1.2. Thermal Etching

For the microstructural characterization of the different designs, samples were thermally etched using the same furnace employed for sintering. The thermal etching process affects the grain boundaries and thus allows the identification of microstructures (grains, second phases) using Scanning Electron Microscopy. The heating profile was similar to the one used for the sintering process. The maximal temperature for the thermal etching process was 1450 °C and the dwelling time was 30 minutes, see thermal profile in Figure 18.

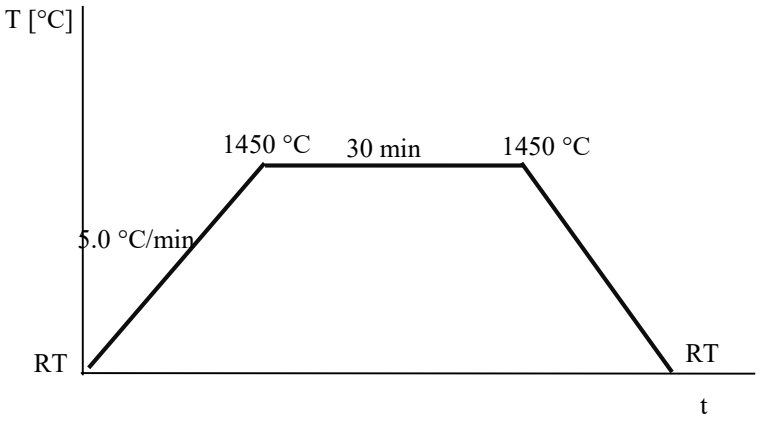

Figure 18. Diagram of the Thermal Etching process

3.3.1.3. Notching of samples for K_{IC} Testing

For the evaluation of the K_{IC} the Single-Edged V-Notched beam test was employed according to the standards of ISO 23146 [38]. The specimen was notched perpendicular to the polished surface using a razor blade and diamond paste, see Figure 19, with a self-made preparation assembly similar to that used by NISHIDA *et al* [39].

First, a coarse notch was made, with a depth of about 0.6 mm, using a diamond paste with a particle size of 6 µm. After reaching this depth, a new razor blade with a diamond paste of 1 µm was applied to induce the tip of the notch, resulting in a smaller notch-radius of approximately 10 µm. This notching procedure was performed on 3 specimens for each monolithic design (non-textured and textured).

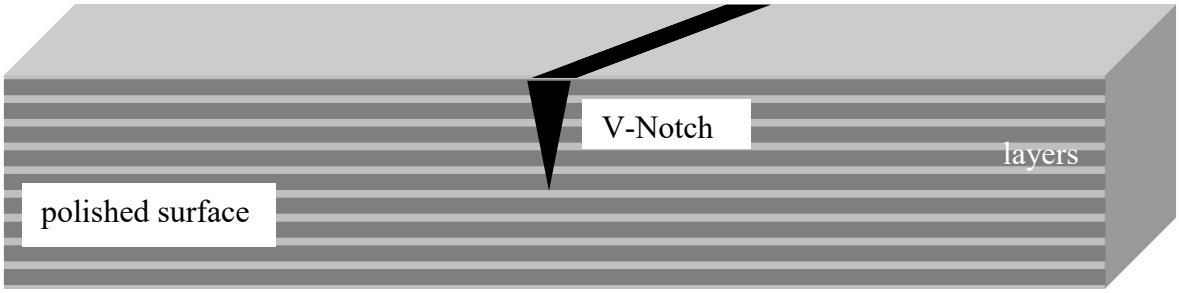

Figure 19. V-Notch perpendicular to the polished surface

3.3.1.4. Chamfering of samples for 4-Point-Bending Testing

For the evaluation of the mechanical strength the prismatic bars were tested via 4-point-bending (4PB) following the standards EN 843-1 [40]. The side of the specimens to be loaded under tension was chamfered on two edges 0.5x0.5 mm with an angle of 45 °, see Figure 20.

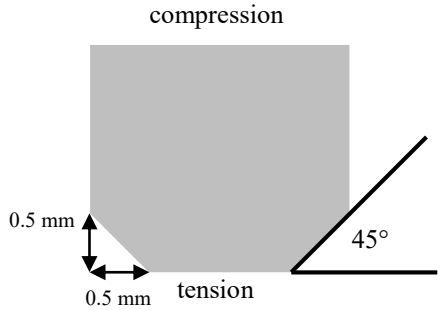

Figure 20. Cross section of a with 45 ° chamfered sample, showing the referred tensile and compressive surface

3.3.1.5. Insertion of artificial indents for indentation fracture strength

In order to study the effect of the different layers on the resistance to crack propagation, indents were artificially inserted on the tensile side of the specimens during bending. For this purpose, indentations using three different loads were made with a Vickers indenter. The applied loads were 2, 5 and 10 kg, which were placed in the middle area of the sample, so that they are located in between the loading rollers during the bending tests.

3.3.2. Evaluation of thermo-physical properties

The thermo-physical properties were evaluated on monolithic and laminated samples. Density and Elastic modulus (*E*) were determined in all materials of study and the Coefficient of thermal Expansion (*CTE*) for only the monolithic materials.

3.3.2.1. Density measurements

For density measurements the Archimedes method was used. Depending on whether the material measured is porous or dense different weights have to be taken in account. Whereas for dense materials the sample is only weighed dry and in liquid, materials containing pores also have to be weighed in air when they are saturated with liquid.

The liquid used for the density measurements was DI-H_2O having a density (ρ_l) of 1 g/cm^3.

Porous materials are defined to have an open porosity resulting in a relative density <95 %. For density calculations the following equation was applied [41]:

$$\rho_b[\mathrm{g/cm^3}] = \frac{m_d \times \rho_l}{(m_s - m_l)} \quad (5)$$

where m_d is the mass of dry sample measured in air in [g], m_l is the mass of sample suspended in liquid in [g], and m_s is the mass of sample saturated with liquid measured in air in [g].

To obtain the relative density (ρ_{rel}), the calculated bulk density (ρ_b) of the material has to be divided by the theoretical density (ρ_{th}):

$$\rho_{rel}[\%] = \frac{\rho_b}{\rho_{th}} \times 100 \quad (6)$$

3.3.2.2. Elastic modulus

For determining the Young's modulus, three prismatic bar specimens of each design were tested under 3-point bending (3PB), with as span of 40 mm, using a universal testing machine (Messphysik Microstrain, Messphysik Materials Testing GmbH, 8280 Fürstenfeld, Austria).

The maximum applied load for the tests of the E-modulus corresponded to approximately 40 to 50 % of the fracture strength of the material, as measured on previously tested samples. The maximum applied load for the different designs are listed in Table 5.

Table 5: Listing of the used maximum loads for determining the E-modulus

Design	Maximum Load
Equiaxed Alumina (EA)	40 N
Textured Alumina (TA)	40 N
Periodic Design (P)	20 N
Non-Periodic Design 1 (NP1)	20 N
Non-Periodic Design 2 (NP2)	80 N

The tests were run with a load cell of 100 N. First an initial load of 1 N was applied with a displacement rate of 0.1 mm/min. The further tests happened with a faster displacement rate of 0.2 mm/min until the set maximum load was achieved, load relief followed. Figure 21 shows the direction of the applied load for monoliths and laminates.

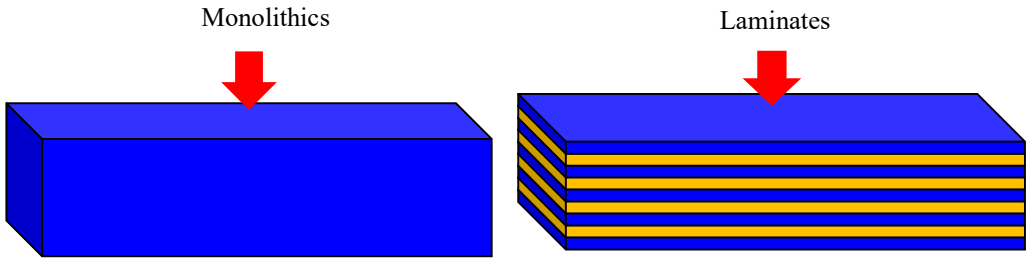

Figure 21. Direction of load for monoliths and laminates

3.3.2.3. Coefficient of thermal expansion

The Coefficient of thermal expansion (*CTE*) was determined only for the monolithic materials in the sintered stage via dilatometry. For the measurements the specimens were

cut into the dimensions 25x3x3 mm. Two samples of the equiaxed and two of the textured Alumina were measured. The specimens were heated from 20 °C up to 930 °C with a heating rate of 2.0 K/min and then cooled with a cooling rate of 2.0 K/min back to room temperature. For the measuring of the thermal expansion of the different monolithic materials the dilatometer Netzsch 402E (Netzsch – Thermal Analysis, 95100 Selb, Germany) was used.

3.3.3. Evaluation of mechanical properties

Hardness, fracture toughness and strength were evaluated in the different monoliths and laminates in order to study the effect of microstructure (non-texture versus texture) and architecture on the mechanical response.

3.3.3.1. Vickers Hardness Testing

The evaluation of the Vickers Hardness was accomplished only on the monolithic materials: (i) equiaxial and (ii) textured alumina. The indented surface was previously polished with diamond paste for a better identification of the imprint of the indent. In the case of the textured samples, two surfaces were indented in order to investigate the effect of the morphology of the textured grains on the mechanical properties (see Figure 22).

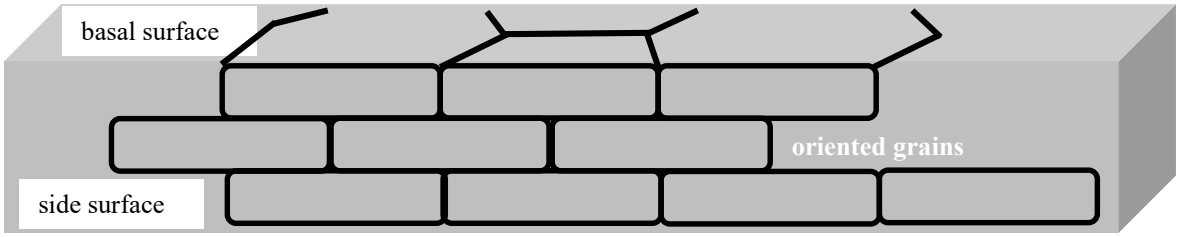

Figure 22. Labelling of the different surfaces of the textured samples; Vickers indents were inserted on the polished side surface

For the tests of the Vickers hardness a Zwick Indenter machine (Zwick 3212B GmbH&Co, 7900 Ulm, Germany) was utilized.

For a statistically significant result, ten intents were made at four different loads (2, 5, 10 and 20 kg) to account for the Indentation Size Effect (ISE) in the material. The hardness evaluation was carried out according to the standards EN 843-4 [42] using a TestXpert analysis Software.

3.3.3.2. Fracture toughness: Single Edge V-Notched beam method

The determination of the fracture toughness was accomplished after the Single Edge V-Notched beam method (ISO 23146) [38]. In this method, a sharp V-notch is introduced in the specimen, on the side to be loaded under tension. A total of 5 samples of both the equiaxed and the textured material were tested under 4PB (with a span 30 – 15 mm), using a Zwick Z010 (Zwick GmbH &Co, 7900 Ulm, Germany) and the data analyzed with TestXpertII software. After setting an initial load of 5 N the test was run with a displacement rate of 1 mm/min till fracture using a load cell of 1 kN. All tests were performed at room temperature and in air.

3.3.3.3. Mechanical strength: natural and artificial (indentation) flaws

The mechanical strength of the different designs was evaluated on samples containing: (i) natural flaws and (ii) artificial (indentation) flaws introduced with a Vickers indenter. The aim of testing natural flaws is to determine what kinds of defects are present and how they interact with the layers of the different designs. For the case of the indented flaws, the objective was to observe the interaction of cracks with the textured microstructure and the compressive stresses in the layers. Both tests were performed on a 4-point bending setting as seen in Figure 23. A schematic of the resulting (maximal) in-plane tensile and compressive stresses during bending is shown.

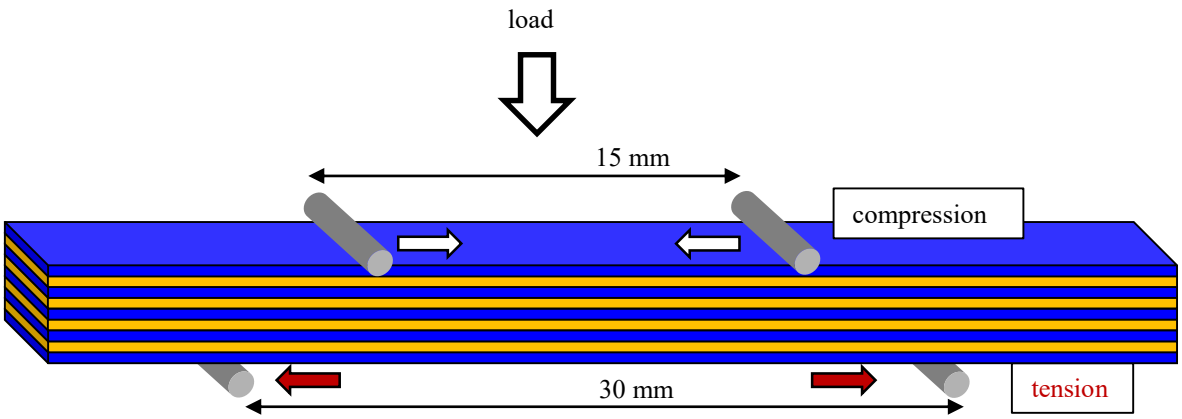

Figure 23. Schematic of the 4PB setting (span 30/15 mm) with the resulting stresses (compression and tension) relating to the load direction on a laminated sample.

1. Mechanical strength of samples with natural flaws

First, the mechanical strength of samples was measured, only including natural flaws. In order to ensure that no flaws from the edges would cause failure during the tests, the edges were chamfered, as described in 3.3.1.4. A universal testing machine (Messphysik Microstrain) was employed with a 1 kN load cell and a 30/15 mm 4PB jig. After reaching an initial preload of 5 N, tests were performed at a displacement rate of 0.5 mm/min. The tests were run in two different orientations, parallel and normal to the stacked layers (referred to as "normal_n" and "parallel_II"). Accordingly the corresponding edges under tension were chamfered, see Figure 24.

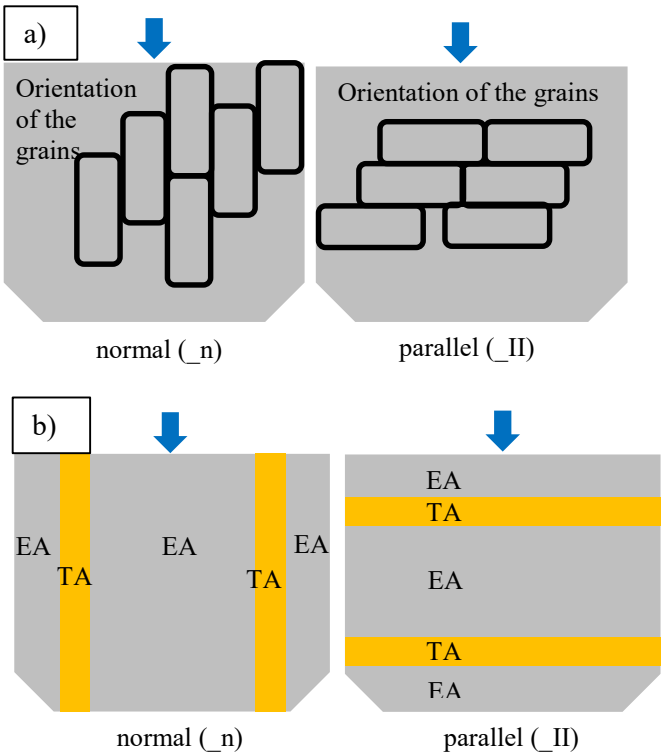

Figure 24. Description of the orientation of the chamfered edged according to the load direction and the direction of the stacked layers of the samples; **a)** shows textured Alumina as example for the normal and parallel orientation for the monolithic samples and **b)** is the representative example for the laminated samples with the non-periodic design

Samples containing between 8 and 10 specimens were tested for all designs: (i) monolithic materials (i.e. equiaxed and textured alumina), (ii) laminated designs (periodic, non-periodic 1, and non-periodic 2) under normal and perpendicular orientation.

2. Mechanical strength of samples with artificial flaws

For the indentation fracture strength, samples were tested in two different directions (named as “normal_n” and “parallel_II”), similar to the samples with natural flaws. Indents were made with the Vickers pyramid on the upper surface, as well as on the side surface (Figure 25). The testing set-up was similar to that used for the samples with natural flaws. A universal testing machine (Messphysik Microstrain) was employed with a 1 kN load cell and a 30/15 mm 4PB jig. After reaching an initial preload of 5 N, tests were performed at a displacement rate of 0.1 mm/min: the smaller rate was chosen to better identify any event (e.g. crack initiation or propagation) during loading. The number of tested samples varied from 3 to 5 for each material, design and orientation.

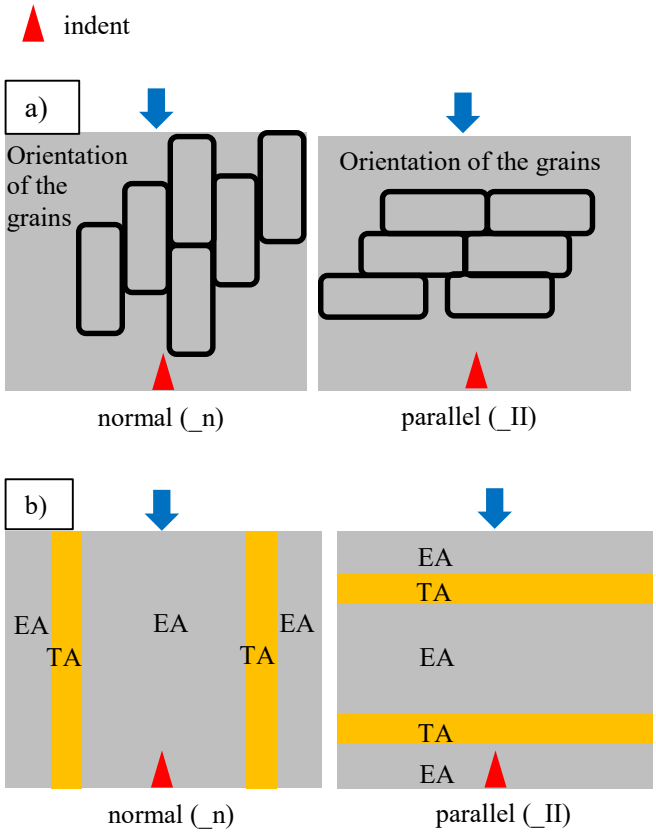

Figure 25. Schematic of the orientation of the stacked layers according to the indent and the applied load; **a)** textured Alumina showing the orientation in the monolithic samples and **b)** normal and parallel orientation for the case of the non-periodic design.

4. Results and discussion

4.1. Microstructural characterization

For the microstructural characterization of the samples, optical and scanning electron microscopy (SEM) was conducted. Furthermore, to determine the degree of orientation in textured samples, X-Ray diffraction was utilized.

4.1.1. Optical and scanning electron microscopy (SEM)

Figure 26 shows three images taken with a scanning electron microscope (Model Quanta 200, FEI, Hillsboro, OR, USA). Figure 26a) displays a microstructure of an equiaxed material (containing alumina and zirconia phases), where the mean grain size is ~2 µm for the alumina and ~0.5 µm for the zirconia phase. For comparison Figure 26b) shows a microstructure of a textured alumina, where the grains have a higher aspect ratio, with an estimated length of ~15-20 µm and a width of ~5 µm. Additionally Figure 26c) presents an interface between two layers containing two different materials with a non-textured and a textured microstructure, respectively.

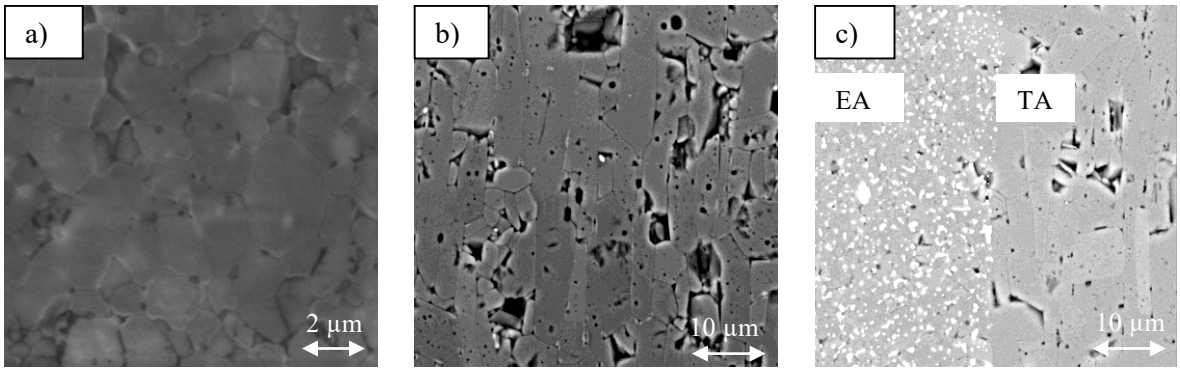

Figure 26. SEM images of representative microstructures of **a)** equiaxed alumina, **b)** textured alumina and **c)** an interface of equiaxed and textured alumina

Additionally, it was observed that the textured microstructure showed a higher volume of pores and “plug-outs”, in comparison to the non-textured material. This might be a result from the liquid phase sintering (LPS) process, which was only applied for the textured samples. During sintering, the liquid phase induces templated grain growth (TGG), where small particles are able to dissolve and precipitate onto the added (larger) templates. Hence, these templates grow at the expense of the smaller particles. Due to the rearrangement of the

particles, liquid phase was probably entrapped, resulting in retained pores after the binder burn-out. Additionally, the arising mobility of the solid material due to the liquid phase might have caused a disruptive reorientation of the templates, maybe leading to an interference of the grain growth, resulting in pores [19,43].

In order to measure the thickness of the sintered samples, an optical microscope (Model BX50, Olympus, Shinjuku, Tokio, Japan) was employed. Results are listed in Table 6, corresponding to the individual layers in Figure 27.

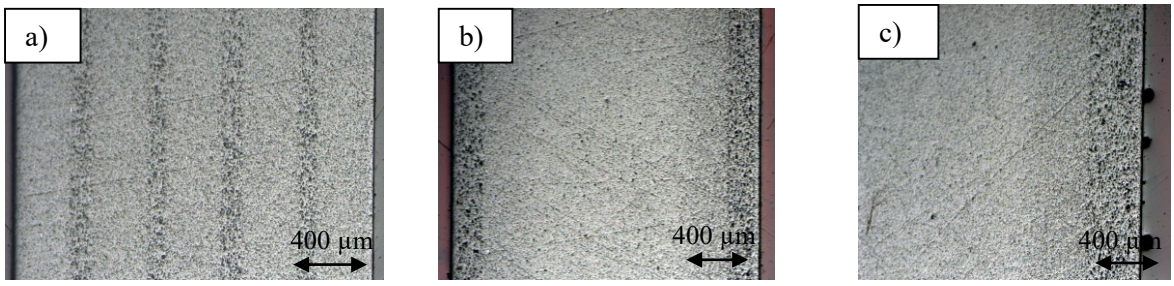

Figure 27. Optical Microscope pictures of layered architectures: **a)** periodic, **b)** non-periodic: design 1, **c)** non-periodic: design 2

Table 6: List of desired and actual thickness of the layers in the laminated samples

		#	Desired thickness of layer [µm]	Actual thickness of layer [µm]
Periodic	layer	1	360	327
		2	75	93
		3	360	294
		4	75	119
		5	360	320
		6	75	116
		7	360	325
		8	75	129
		9	360	319
Non-periodic 1	layer	1	50	42
		2	150	153
		3	1700	1606
		4	150	144
		5	50	49
Non-periodic 2	layer	1	50	43
		2	250	311
		3	2900	2695
		4	250	398
		5	50	52

[1] a factor for the variations of the desired thicknesses compared to the actual thicknesses can be the variation of the thicknesses of the fabricated tapes, due to the not automated process

4.1.2. Texture degree in monoliths and laminates

During templated grain growth the basal plane (0001) of the hexagonal crystal structure is oriented parallel to the surface of a sample, perpendicular to the c-axis in the crystal, see hexagonal crystal structure in Figure 28.

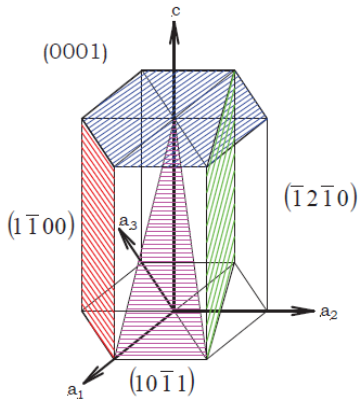

Figure 28. Hexagonal crystal structure showing the (0001) plane [9]

The quality and degree of texture in the different samples was analyzed via X-Ray diffraction. Figure 29 shows the X-Ray diffraction patterns in textured and equiaxed alumina samples. In the textured material, see Figure 29a), two very significant peaks in two of the (000z) directions, i.e. ((0006) and (000 12)) were observed, whereas in a randomly oriented alumina, see Figure 29b) those peaks are hardly observable. Considering the height of these two peaks the degree of orientation in the textured material can be determined calculating the so-called Lotgering factor (*LF*) [24].

$$LF = \frac{p - p_0}{1 - p_0} \tag{7}$$

$$p = \frac{textured\ peaks\ of\ textured\ sample}{sum\ of\ all\ peaks\ of\ textured\ sample}$$

$$p_0 = \frac{textured\ peaks\ of\ random\ sample}{sum\ of\ all\ peaks\ of\ random\ sample}$$

For the calculation of the Lotgering factor a XRD-pattern of a randomly oriented pure alumina was taken as a reference, see Figure 29b). As already mentioned the LF gives states the degree of orientation in a textured material, meaning the higher LF, the better the orientation of the grain perpendicular to the c-axis. Table 7 shows the calculated LFs for the fabricated textured samples in this study.

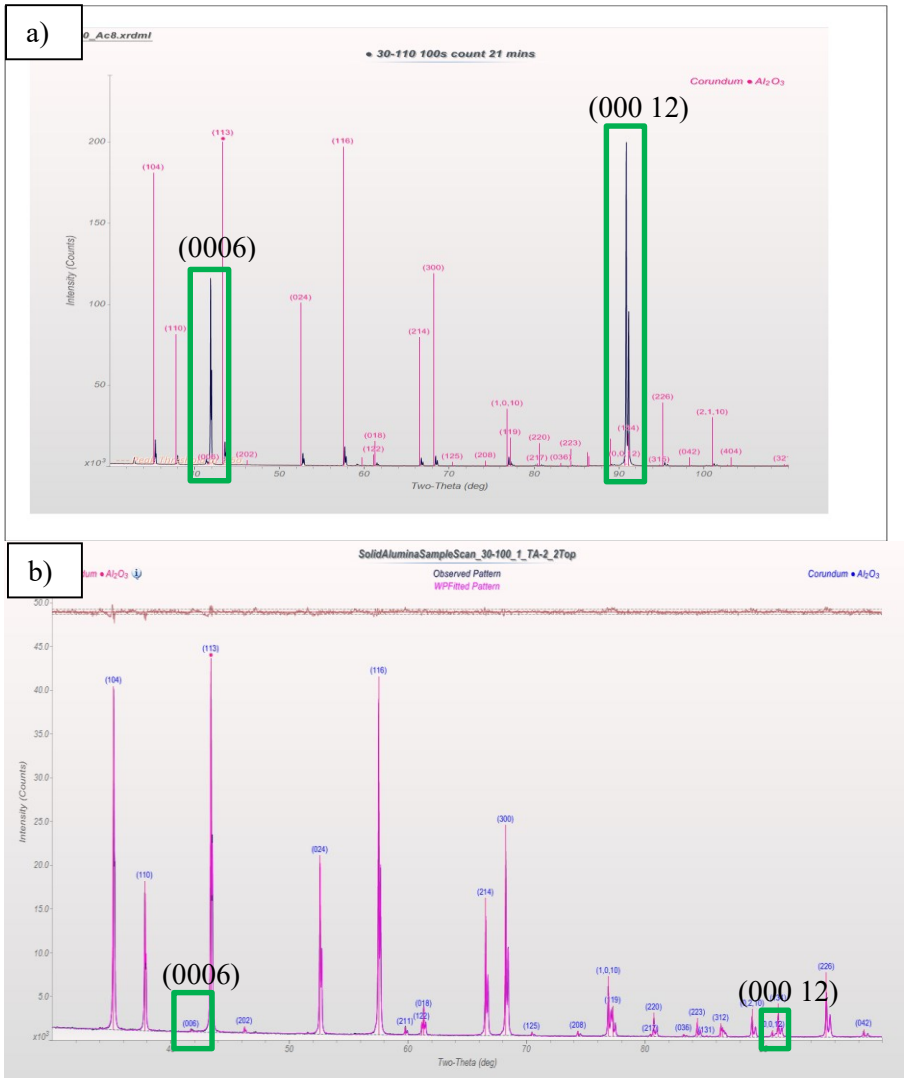

Figure 29. XRD diffraction patterns of **a)** textured and **b)** randomly oriented alumina

Table 7: Lotgering factors of selected fabricated textured alumina samples

sample	#	LF [%]
TA30-Ac2,3	1	43.62
TA30-Ac4_1	2	66.00
TA30-Ac4_2	3	71.78
TA30-Ac6	4	41.60
TA30-Ac8	5	71.65

4.2. Physical Properties

4.2.1. Dimensions and shrinkage behavior of monoliths and layered samples

In order to determine the shrinkage of the materials, sample dimensions (a1: width, a2: length, h: thickness) were measured after the different processing steps. Table 8 displays the average values for the dimension measurements of the different designs: (i) EA: equiaxed alumina, (ii) TA: textured alumina, (iii) P: periodic laminate, and (iv) NP: non-periodic laminate.

Table 8: Length (a1), width (a2) and height (h) of the different samples, along with the shrinkage calculations

design	dimensions	a_1	$\Delta a_1(a_x-a_0)$		a_2	$\Delta a_2(a_x-a_0)$		h	$\Delta h(h_x-h_0)$	
		[mm]	[mm]	[%]	[mm]	[mm]	[%]	[mm]	[mm]	[%]
EA	HP/IP	50.54			50.62			3.80		
	after BB-Out	50.47	-0.07	-0.13	50.69	0.06	0.13	3.77	-0.03	-0.88
	after CIP/sintering	41.52	-8.95	-17.74	41.33	-9.36	-18.46	3.07	-0.70	-18.48
	total shrinkage		-9.02	-17.85		-9.30	-18.36		-0.73	-19.19
design	dimensions	a_1	$\Delta a_1(a_x-a_0)$		a_2	$\Delta a_2(a_x-a_0)$		h	$\Delta h(h_x-h_0)$	
		[mm]	[mm]	[%]	[mm]	[mm]	[%]	[mm]	[mm]	[%]
TA	HP/IP	50.32			50.70			3.88		
	after BB-Out	50.44	0.12	0.23	50.55	-0.15	-0.30	3.78	-0.10	-2.61
	after CIP/sintering	44.19	-6.25	-12.38	44.43	-6.13	-12.12	3.02	-0.77	-20.26
	total shrinkage		-6.13	-12.18		-6.28	-12.38		-0.87	-22.35
design	dimensions	a_1	$\Delta a_1(a_x-a_0)$		a_2	$\Delta a_2(a_x-a_0)$		h	$\Delta h(h_x-h_0)$	
		[mm]	[mm]	[%]	[mm]	[mm]	[%]	[mm]	[mm]	[%]
P	HP/IP	50.45			50.34			2.79		
	after BB-Out	50.25	-0.20	-0.39	49.91	-0.43	-0.85	2.82	0.04	1.35
	after CIP/sintering	42.02	-8.24	-16.39	41.82	-8.08	-16.20	2.23	-0.59	-20.95
	total shrinkage		-8.44	-16.72		-8.51	-16.92		-0.55	-19.88
design	dimensions	a_1	$\Delta a_1(a_x-a_0)$		a_2	$\Delta a_2(a_x-a_0)$		h	$\Delta h(h_x-h_0)$	
		[mm]	[mm]	[%]	[mm]	[mm]	[%]	[mm]	[mm]	[%]
NP	HP/IP	50.24			50.18			3.12		
	after BB-Out	50.00	-0.24	-0.47	49.94	-0.24	-0.49	3.07	-0.05	-1.60
	after CIP/sintering	41.65	-8.35	-16.70	41.56	-8.38	-16.79	2.41	-0.66	-21.52
	total shrinkage		-8.58	-17.09		8.63	-17.19		-0.71	-22.78

Examining the shrinkage occurring during different processing steps, it is observed that the largest dimensional change takes place during sintering. This is due to densification according to the sintering mechanisms as described in 1.2. When observing the stage of Binder-Burn-Out only a small shrinkage occurs, because here only the polymer phase is removed, without any changes on the inorganic phase. The result is a skeleton of sensitive ceramic, which experiences shrinkage during sintering.

Comparing the shrinkage in different directions, it can be seen that in the equiaxed design the changes in width, length and height are approximately the same. In contrast to that, especially for the textured monolithic design, there is a significantly higher total shrinkage in height (i.e. -22.35 %) than in width and length (i.e. approx. -12 %).

The reason for this difference is described as a result of the rearrangement of the tailored grains. While in the equiaxed material grains grow in no preferential direction, in the textured material grain growth occurs preferentially along the oriented templates in the a1- and a2-direction.

4.2.2. Density

The theoretical density for alumina $\rho_{th}(Al_2O_3)$ is 3.986 g/cm^3 [32], and for zirconia $\rho_{th}(ZrO_2)$ = 6.05 g/cm^3 [44]. For the non-textured material, the theoretical density was calculated as a combination of the theoretical densities of alumina and zirconia, due to the composition of 95% alumina and 5% zirconia. Accordingly, the theoretical density for the non-textured material $\rho_{th}(Al_2O_3+ZrO_2)$ was 4.089 g/cm^3.

Table 9 shows the average values of the density measurements and the calculated densities and relative densities through equation (1) and (2), respectively, for the non-textured (EA) and textured (TA) monolithic samples.

Table 9: Measured masses and density calculations [32,44]

material	# of samples	m_d	m_l	m_s	ρ_b	ρ_{th}	ρ_{rel}
		[g]	[g]	[g]	[g/cm^3]	[g/cm^3]	[%]
EA	6	20.1463	15.1766	20.1758	4.030	4.089	98.55
TA	5	20.4324	15.1748	20.5093	3.830	3.986	96.09

A relative high density could be obtained for both equiaxed and textured materials, with ~98.5 % and ~96.1 % of the theoretical density, respectively. The lower density in the textured material can be explained by the porosity associated with the liquid phase sintering process (as discussed in section 4.1).

4.2.3. Vickers Hardness (HV)

Figure 30 shows typical indentations of a Vickers indenter with a load of 5 kg on EA and TA samples in two different surfaces. As described in 3.3.3.1. in comparison to the equiaxed monoliths, where the grains are randomly oriented, the different surfaces of the textured alumina samples may show different mechanical behavior, related to the orientation of the templated grains.

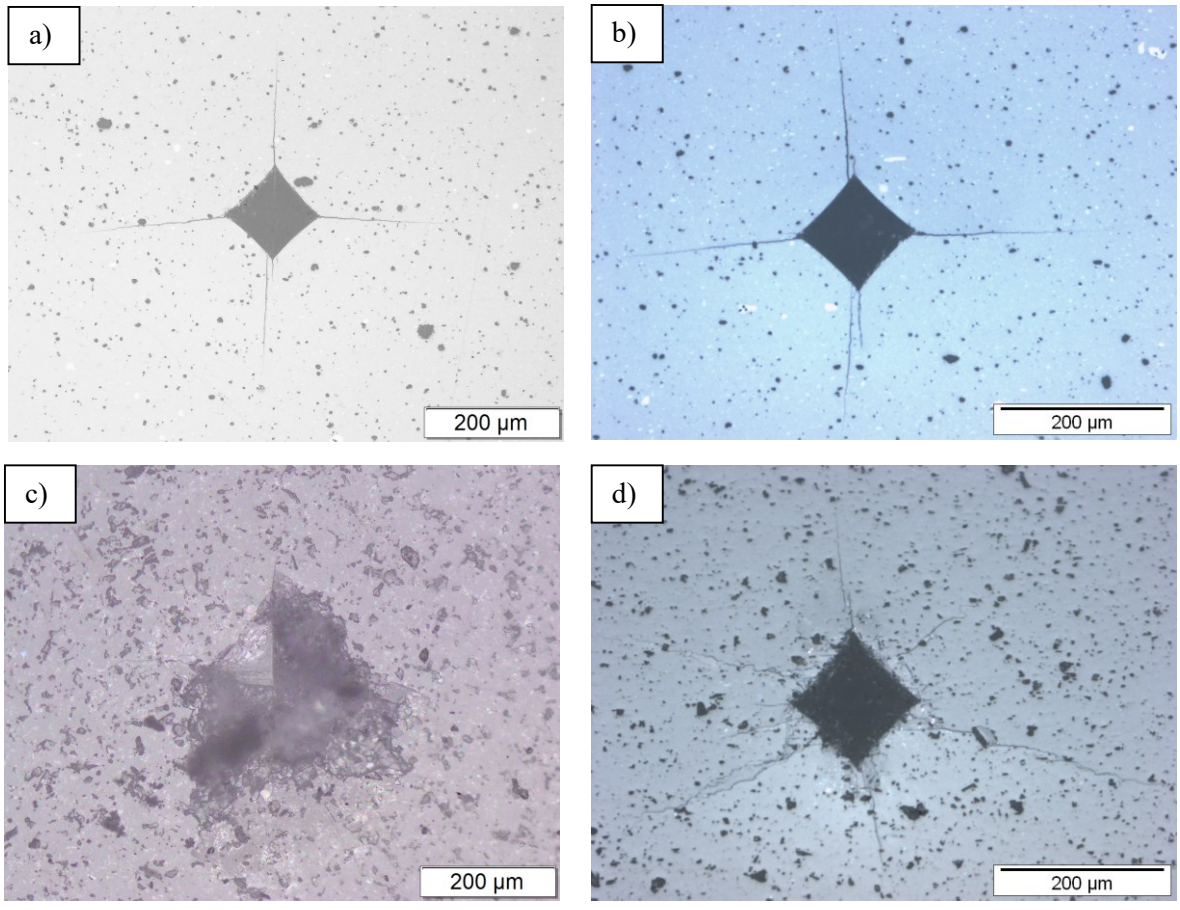

Figure 30. Vickers Indentations of **a)** EA monoliths on the basal surface, **b)** EA monoliths on the side surface, **c)** TA monoliths on the basal surface and **d)** TA monoliths on the side surface.

The indentations in Figure 30a) and b) displays the response of the EA material to the applied indenter load. Both indents are similar, showing (as expected) no significant difference between the two surfaces. Figure 30c) and d) show the imprints corresponding to indentation on two different surfaces of the TA material. In the case of Figure 30c) the basal planes of the grains are perpendicular to the applied load. The spallation of material at the basal surface is probably caused by the tailored grains, which work against the applied load by sliding, instead of deforming inelastically, and thus causing delamination of templates. Those indentations were marked as invalid for hardness measurements. Figure 30d) shows an indent on the other surface of the TA material. The imprint is here well defined, although cracks are emanating from different locations and not from the corner of the indent, as expected in a brittle material. This may be also associated with the effect of the templated grains and thus the anisotropy of the TA material.

The resulting values for the Vickers hardness at different loads were calculated as followed:

$$HV\ [kp] = \frac{1}{g}\frac{F \cdot 2 \cdot sin\frac{136^\circ}{2}}{d^2} \approx 0.1891 \cdot \frac{F}{d^2} \quad (8)$$

where g = 9.81 m/s^2 is the gravity, F is the applied load in [N], sin(136°/2) is the angle of the Vickers indenter and d represents the arithmetic average of the two diagonal distances in [mm] [42,45].

The determined values of Vickers Hardness for non-textured and textured materials are plotted in Figure 31. The higher hardness of the equiaxied material was expected due to the relatively smaller grain sizes and the randomly oriented microstructure in contrast to the textured material. Further, another influence for the lower hardness for the textured monoliths can be the high porosity ($\rho_{porosity,\ TA}$ = 3.91 %) and the surface on which the indentations were made. This might be due to the lower hardness of hexagonal single crystals in the direction perpendicular to the side planes [25,26].

Additionally, to the difference in hardness of the two different materials, the indentation size effect could be observed. This effect describes the decreasing hardness values with increasing applied load, as seen in Figure 31 [46], being affected by the grain boundaries.

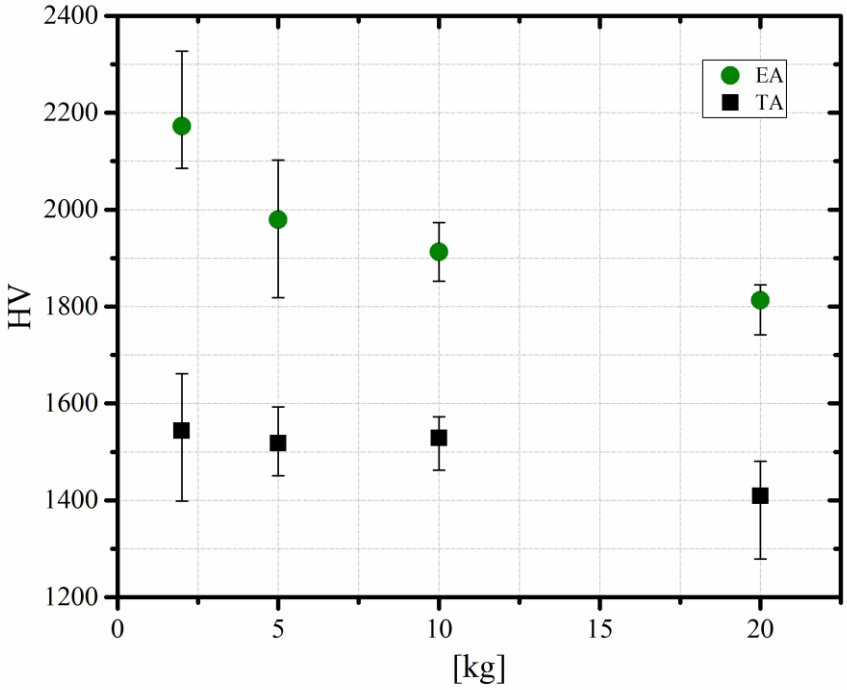

Figure 31. Comparison of the measured Vickers Hardness for the monoliths: (i) equiaxial and (ii) textured alumina.

4.2.4. E-modulus of monoliths and laminates

The Young's modulus was measured for the monolithic samples as well as for the laminates, as described in 3.3.2.2. The measured and theoretical E-moduli are listed in Table 10. For the comparison of the measured Young's modulus of equiaxed and textured monoliths with a theoretical value, a specification from literature for a ~99 % pure alumina was taken in account [3,9]. The theoretical E-modulus for the laminates was estimated following the rules of mixtures, taking into account a "parallel connection" according to the loading configuration used for the measurement (see Figure 21). The effective theoretical E-modulus of the layered samples was determined with the following equation:

$$E_{laminates}[GPa] = \frac{1}{\frac{V_{EA}}{E_{EA}} + \frac{V_{TA}}{E_{TA}}} \quad (9)$$

[48]

where V_{EA} and V_{TA} are the fractions of volume for equiaxed and textured alumina layers and E_{EA} and E_{TA} are the Young's moduli of the measured monolithic materials.

Since the volume ratio is the same for all the three different laminated designs (=1:6) the calculated value, i.e. 379 ± 10 GPa, is representative for the periodic and the non-periodic designs.

Table 10: Evaluated E-moduli for the different designs in comparison to E-moduli found in the literature and after calculation for the laminated samples

design	measured E-moduli	theoretical E-moduli
	[GPa]	[GPa]
EA	380 ± 12	380 - 405 [3,9]
TA	381 ± 6	
P	350 ± 26	379 ± 10
NP1	381 ± 4	
NP2	379 ± 9	

The measured E-modulus of the monolithic samples (EA and TA) is in good agreement with the theoretical values. The Young's modulus of the periodic laminates (P) is significantly lower than that of the non-periodic laminates (NP1 and NP2). This could be due to the higher number of interfaces between the equiaxed and textured layers. The bonding in these interfaces might be weaker, resulting in more compliance, thus smaller E-modulus. Additionally, the periodic samples showed a curvature, which probably additionally effected the resulting as tested Young's modulus.

4.2.5. Coefficient of Thermal Expansion (CTE)

The *CTE* (α) of the monolithic materials (EA and TA) was determined via dilatometry on already sintered samples. Figure 32 shows the change in length, ΔL, with respect to the initial length, L_0, as a function of temperature, for two representative equiaxed (EA) and textured (TA) samples.

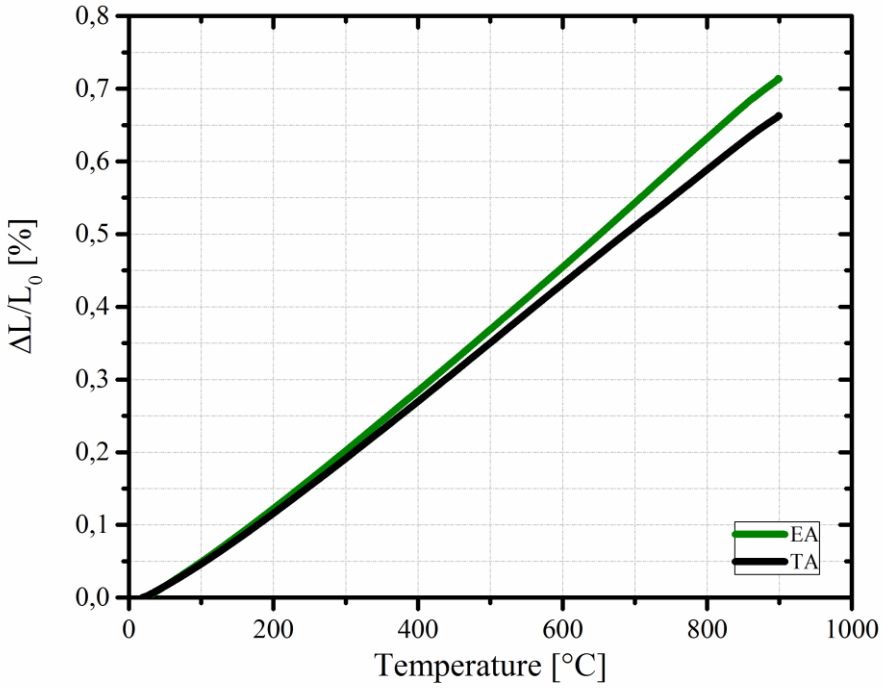

Figure 32. Comparison of the dilatometry curves for the textured (TA) and equiaxial (EA) materials

The heating was performed from 20 °C up to 930 °C. The evaluation of the coefficient of thermal expansion was made for the temperature range between 20 °C and 850 °C. The resulting technical *CTE*s are listed in Table 11 which were evaluated as followed:

Fitting of the dimensional change ($\Delta L/L_0$) in dependence of the difference in temperature, via a second order polynomic function:

$$\frac{\Delta L(T,T_{ref})}{L_0} = \varepsilon_{therm}(T,T_{ref})\big|_{T_{ref}} = a\left(T - T_{ref}\right) + b(T - T_{ref})^2 \qquad (10)$$

where a and b are non-dimensional coefficients, T is the observed temperature in [°C] and T_{ref} is the reference temperature in [°C].

The first deviation of (10) results in the differential CTE (α_{diff}) as followed:

$$\alpha_{diff}(T) = \frac{d\varepsilon_{therm}(T,T_{ref})\big|_{T_{ref}}}{dT} = a + 2b(T - T_{ref}) \qquad (11)$$

For the evaluation of the technical CTE (α_{tech}) equation (11) is integrated over the desired temperature range:

$$\alpha_{tech}(T, T_{ref})\big|_{T_{ref}} = \frac{1}{T - T_{ref}} \cdot \int_{T_{ref}}^{T} \alpha(T') \cdot dT' = a + b(T - T_{ref}) \qquad (12)$$

Table 11: List of evaluated technical *CTE*s (α) (Temp. range: 20-850 °C) for the monolithic materials (i) EA and (ii) TA

material	CTE (α)
	10^{-6} [K^{-1}]
EA	8.24 ±0.07
TA	7.82 ±0.10

It can be observed that the *CTE* of the equiaxial material is slightly higher than that of the textured material. This results from the additional zirconia in the equiaxed alumina, which has a significantly higher *CTE* than alumina, i.e. $\alpha(ZrO_2) \approx$ 10E-6 K^{-1} [34]

Additionally, the different microstructures might have an influence on the measured *CTE*. Since, the EA probably expands in all dimensions similar, the expansion of the tailored grains in the TA might differ depending on the orientation of the sample [15,16].

4.2.6. K_{IC} of monoliths

The fracture toughness (K_{IC}) for the monolithic materials (EA and TA) was evaluated according to the SEVNB method as described in 3.3.1.3. and 3.3.3.2. [38]. The K_{IC} values were calculated using the following equation:

$$K_{IC} = \frac{F_{max}}{b \cdot \sqrt{h}} \cdot \frac{L - l}{h} \cdot \frac{3 \cdot \sqrt{\frac{a}{h}}}{2 \cdot (1 - \frac{a}{h})^{1.5}} \cdot Y^* \qquad (13)$$

where F_{max} is the maximum applied load, b is the width of the tested bar in [mm], h is the height in [mm], L is the bottom span of the testing assembly in [mm], l is the top span in [mm], a is length of the induced V-notch in [mm] and Y^* is the non-dimensional geometrical factor which is calculated as followed, for bar-shaped samples:

$$Y^* = 1.9887 - 1.326 \cdot \frac{a}{h} - \frac{(3.49 - 0.68 \cdot \frac{a}{h} + 1.35 \cdot (\frac{a}{h})^2) \cdot \frac{a}{h} (1 - \frac{a}{h})}{(1 + \frac{a}{h})^2} \qquad (14)$$

[38]

Table 12 shows the K_{IC} values for the equiaxed ($K_{IC,EA}$) and textured ($K_{IC,TA}$) samples. $K_{IC,TA}$ is significantly larger than $K_{IC,EA}$.

Table 12: Fracture toughness for the monolithic materials (i) equiaxed and (ii) textured alumina

monolith	K_{IC}
	[MPam$^{1/2}$]
EA	3.8 ±0.5
TA	4.4 ±0.2

This increase of toughness can be associated with the effect of the templated microstructure, shielding the propagation of the crack in the material. A model can be seen in Figure 33 where deflection and bifurcation mechanisms may take place, as has been observed in other textured materials [22,29,50].

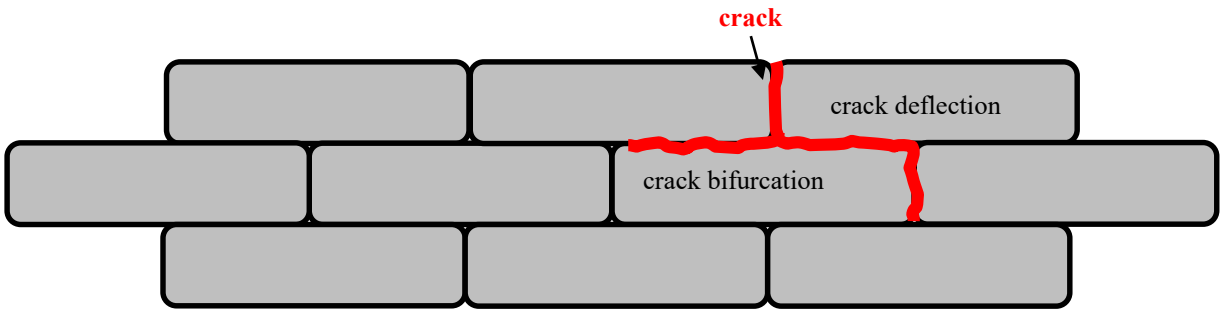

Figure 33. Displaying the effects of crack bifurcation and crack deflection

The crack preferentially propagates along the grain boundaries (intergranular). As a result of the textured microstructure the crack gets deflected parallel to the surface on which the load is applied. This leads to an extended distance the crack has to cover resulting in an increase of the toughness.

Besides the deflection of the cracks it may also occur that, when hitting a basal plane of oriented grains, some cracks can get divided into sub-cracks, also seen in Figure 33. This bifurcation into sub-cracks might also reduce the driving force for the crack growth, leading to a higher K_{IC} in textured materials.

4.3. Estimation of Residual Stresses

The laminates investigated consist of a combination of different layers containing EA and TA materials. Since the layers are strong bonded (i.e. strong interface), residual stresses are generated during cooling from the sintering step due to the different coefficient of thermal expansion between EA and TA materials (see Table 11). As a result, tensile residual stresses will be induced in the equiaxed layers and compressive residual stresses will be generated in the textured layers.

The induced compressive residual stresses are considered to be a key element to enhance the resistance of the laminate to the propagation of cracks, as it has also been demonstrated in other systems [16,51,52]. Under some particular conditions, compressive embedded layers can even arrest the propagation of surface cracks [4,15].

For the laminated designs investigated, it was intended to achieve compressive residual stresses in the textured layers induced through the different *CTE*s of the combined materials (EA and TA). The resulting residual stresses were estimated with the following equations:

$$\sigma_{res,i} = \frac{E_i}{1-\upsilon_i} (\bar{\alpha} - \alpha_i) \Delta T \quad (15)$$

$$\bar{\alpha} = \sum_{i=1}^{N} \frac{E_i t_i \alpha_i}{1-\upsilon_i} / \sum_{i=1}^{N} \frac{E_i t_i}{1-\upsilon_i} \quad (16)$$

[15,29]

where $\sigma_{res,i}$ is the resulting residual stress, E_i represents the E-modulus in [MPa], υ_i the Poisson's ratio, α_i is the *CTE*, $\bar{\alpha}$ stands for the average of the *CTE*s of the different materials and t_i states the thickness of the layer. i is the running index for the numbering of the corresponding layer.

The materials properties were reported in Table 1, Table 10 and Table 11. The Poisson's ratio was taken from the literature as υ=0.22 [15]. In Table 13 the calculated in-plane residual stresses in the EA and TA layers are given.

Table 13: Estimated residual stresses for EA and TA layers

$\sigma_{res, EA}$	45	[MPa]
$\sigma_{res, TA}$	-270	[MPa]

According to the equilibrium of forces, the following relation must hold:

$$\sigma_{TA} \cdot V_{TA} + \sigma_{EA} \cdot V_{EA}=0 \quad (17)$$

As a result, the compressive residual stresses in the textured layers are significantly higher than the tensile residual stresses in the outer equiaxed layers, which is related to the lower volume of TA material in the laminates, i.e. $V_{TA}:V_{EA}$=1:6. It is hypothesized that the compressive residual stresses in the textured layers of the laminates will shield the propagation of surface cracks, affecting the crack path due to the textured microstructure.

4.3.1. Edge Cracking due to residual stresses

The described tensile (EA-layers) and compressive (TA-layers) residual stresses are in-plane (biaxial) stresses far from the free edges of the samples. These stresses are parallel to the layered structure. However, at the free edges, so-called out-of-plane stresses are generated, which are perpendicular to the layer plane leading to tensile stresses on the edges of the compressive layers. The magnitude of the tensile stresses is related to the in-plane compressive stresses. If they reach a certain value, so called “edge cracks” in the textured layers may appear, see Figure 34. This behavior could be observed for laminated samples of the non-periodic designs 1 and 2 (see Figure 34b) and c)), however not for the periodic design (Figure 34a)). The occurrence of edge cracks in the non-periodic designs is due to the higher thickness of the textured layers in comparison to the periodic design. In a recent work, a novel approach was developed to predict the onset and propagation of surface cracks (namely edge cracks) in ceramic laminates [53]. The conditions for crack initiation/propagation were assessed using a stress–energy coupled criterion [54]. For a given thickness of the compressive layer, no edge crack is to initiate for relatively low internal (in-plane) compressive residual stress in the layer. For higher stress values, edge crack may initiate and grow in a stable manner if a certain layer thickness is reached. Figure 35 shows the relation between thickness and residual stresses in ceramic laminates for the onset of edge cracking.

The phenomenon of edge cracking was only found in occasional non-periodic samples. Since, the induced compressive stresses in the textured layers were of a smaller magnitude ($\sigma_{res, TA}$ = -270 MPa) than expected, leading to smaller out-of-plane tensile stresses. Weak out-of-plane tensile stresses might not be able to form edge cracks.

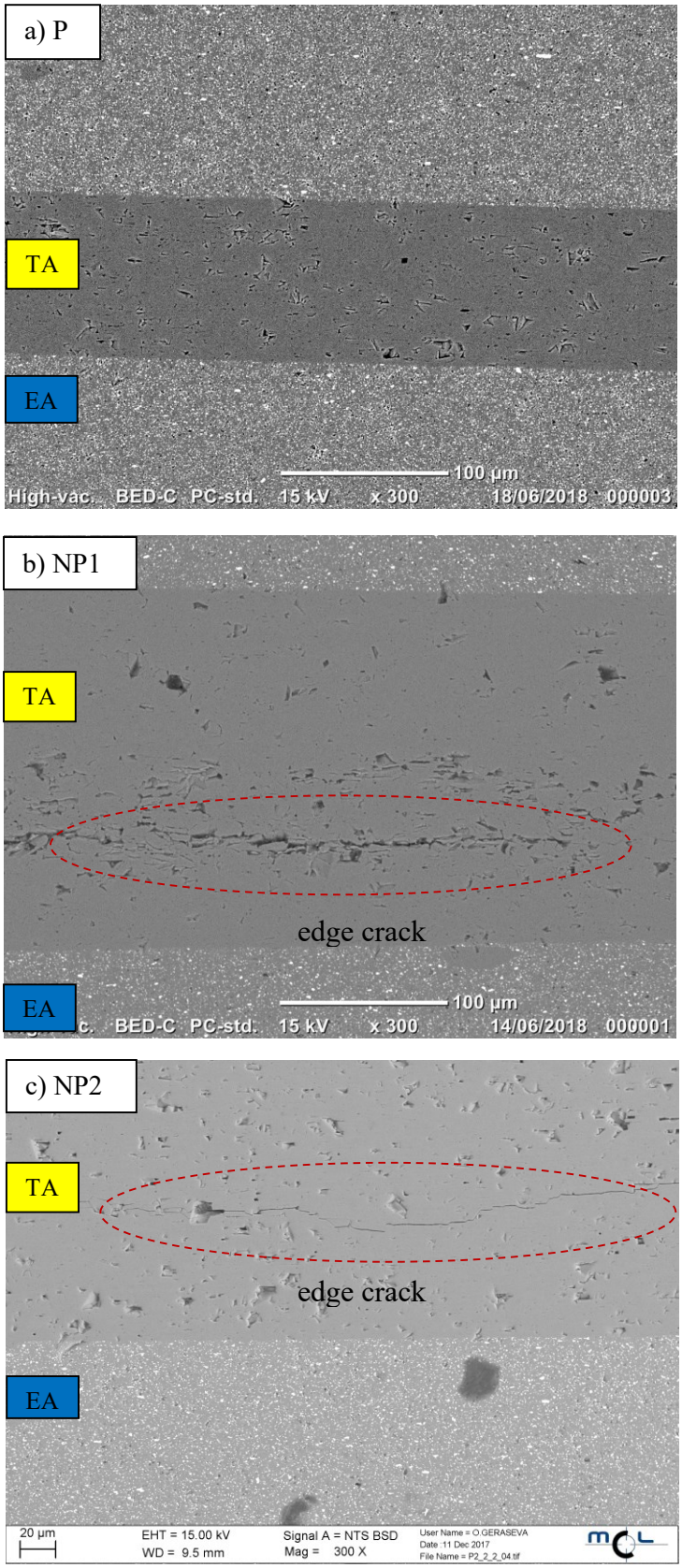

Figure 34. SEM pictures of the different laminated designs: **a)** periodic, **b)** non-periodic 1, **c)** non-periodic 2; determining if edge cracks are present

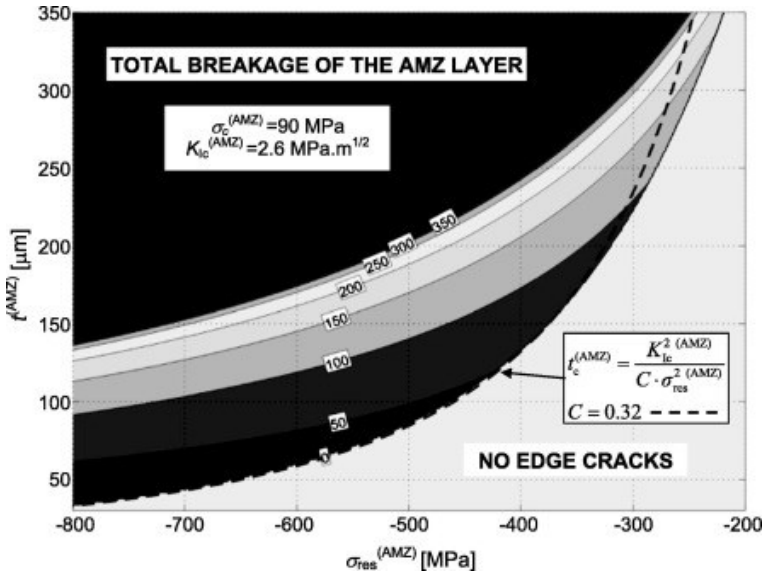

Figure 35. Depths of the edge cracks for a given residual compressive stress in a compressive layer (referred to as AMZ) as function of layer thickness. The numbers in white boxes inside the plot denote the final edge crack depth in μm for certain combination of residual stress and thickness [54].

4.4. Mechanical behavior

4.4.1. Strength of monoliths and laminates

The strength of the monoliths (EA and TA) and the laminates (P, NP1 and NP2) was evaluated via 4PB testing. From the test data for the applied force and the displacement of the crosshead were measured. With the data of the applied force the bending strength of the chamfered samples was evaluated as followed:

$$\sigma_B = \frac{M_{b,max}}{W} \tag{18}$$

where σ_B is the resulting bending strength in [MPa], $M_{b,max}$ is the maximum bending moment in [Nm] and W is the moment of resistance in [mm^3].

The maximum bending moment and the moment of resistance were determined with:

$$M_{b,max} = \frac{F(L-l)}{4} \tag{19}$$

$$W = \frac{I}{a_{max}} \tag{20}$$

where F is the applied force in [N], L is the bottom span of the testing assembly in [mm], l is the top span in [mm], I is the moment of inertia in [mm^4] and a_{max} is the maximum distance between center and edge layer in [mm] [40].

The tested samples were chamfered with 2x45° chamfers on two sides, which were considered in the calculation resulting in a corrected bending strength. The corrected bending strength was evaluated as followed:

$$\sigma_{B,corr} = f \cdot \sigma_B \tag{21}$$

where $\sigma_{B,corr}$ is the corrected bending strength in [MPa], f is the non-dimensional factor of correction and σ_B is the calculated bending strength in [MPa].

The factor of correction considers the width and the length of the induced chamfers and was calculated as described [55]:

$$f = \frac{BH^2(-2c^3+3BH^2)}{3B^2H^4-6BHc^4+12BH^2c^3-12BH^3c^2+2c^6} \tag{22}$$

where B and H are width and height of the samples in [mm] and c is the average length of the chamfer in [mm].

Figure 36 shows representative curves of $\sigma_{B,corr}$ as a function of the crosshead displacement for the monoliths (i) equiaxed alumina (EA) and (ii) textured alumina (TA) as well as for the laminates with the (iii) periodic design (P), (iv) the non-periodic design 1 (NP1) and the non-periodic design 2 (NP2). In Figure 36a) the curves for the samples, tested perpendicular (_n) to the layers are displayed. Figure 36b) shows the curves, where the applied force appeared parallel (_II) to the layers of the samples.

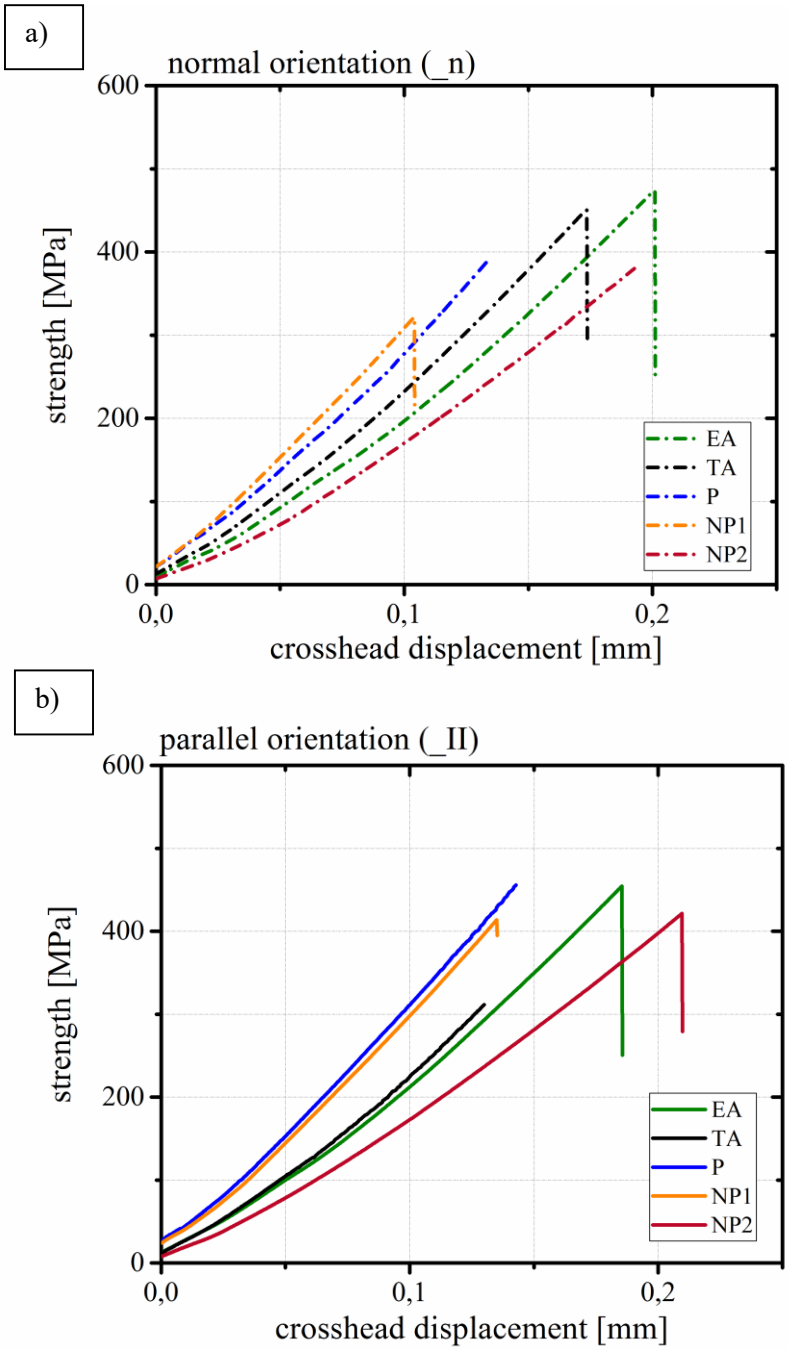

Figure 36. a) shows the representative curves, where the testing direction was perpendicular (_n) to the layers of the samples and **b)** displays the curves of the parallel (_II) orientation.

Further, the probability of failure for the different materials was determined according to the Weibull distribution:

$$F(\sigma) = 1 - \exp[-\left(\frac{\sigma}{\sigma_0}\right)^m] \quad (23)$$

where $F(\sigma)$ is the probability of failure in [%] as a function of the applied stress (σ) in [MPa], σ_0 is the characteristic strength in [MPa] and m represents the Weibull modulus. The Weibull

modulus *m* was evaluated with the Maximum-Likelihood-method, applying the following approximation formula:

$$\frac{\sum_{i=}^{N}[\ln(\sigma_{B,i})\cdot\sigma_{B,i}^{m}]}{\sum_{i=}^{N}\sigma_{B,i}^{m}} - \frac{1}{N}\sum_{i=}^{N}\ln\left(\sigma_{B,i}\right) - \frac{1}{m} = 0 \qquad (24)$$

where N is the total number of tested samples, $\sigma_{B,i}$ represents the corrected bending strength for a particular sample in [MPa] and i is the running index for the number of specimens. The determination of the characteristic strength was accomplished as followed:

$$\sigma_0 = \left[\frac{1}{N}\left(\sum_{i=1}^{N}\sigma_{B,i}^{m}\right)\right]^{1/m} \qquad (25)$$

[56,57]

The evaluated characteristic strengths, their confidence interval, the Weibull-moduli and their confidence interval for the different designs (i) equiaxed alumina (EA), (ii) textured alumina (TA), (iii) periodic design, (iv) non-periodic design 1 and (v) non-periodic design 2 for the two testing directions, (a) perpendicular (_n) and (b) parallel (_II) to the layers are listed in Table 14.

Table 14: Shows the investigated characteristic strength and Weibull modulus with their confidence intervals for the different materials and testing directions

Material	Characteristic strength σ_0 [MPa]	Confidence interval for σ_0	Weibull-modulus m	Confidence interval for m
EA_n	458	421-501	8.7	4.3-12.1
EA_II	437	406-472	10.0	5.0-13.9
TA_n	409	395-424	27.8	11.5-40.2
TA_II	346	336-357	32.5	13.4-46.9
P_n	454	403-514	6.3	3.1-8.7
P_II	450	398-511	6.9	3.1-9.7
NP1_n	311	277-351	5.9	3.1-8.1
NP1_II	383	343-431	6.7	3.3-9.3
NP2_n	376	354-400	12.4	6.1-17.2
NP2_II	381	338-431	5.8	3.0-7.9

Figure 37a) and b) show the Weibull distribution for samples tested a) perpendicular (_n) to the layers and b) parallel (_II) to the layers. In The Weibull distribution, the probability of failure is a function of the maximum corrected bending strength. According to the diagram, the characteristic strength is that, where the line crosses the probability of failure at 63.21 %, as displayed in the graph.

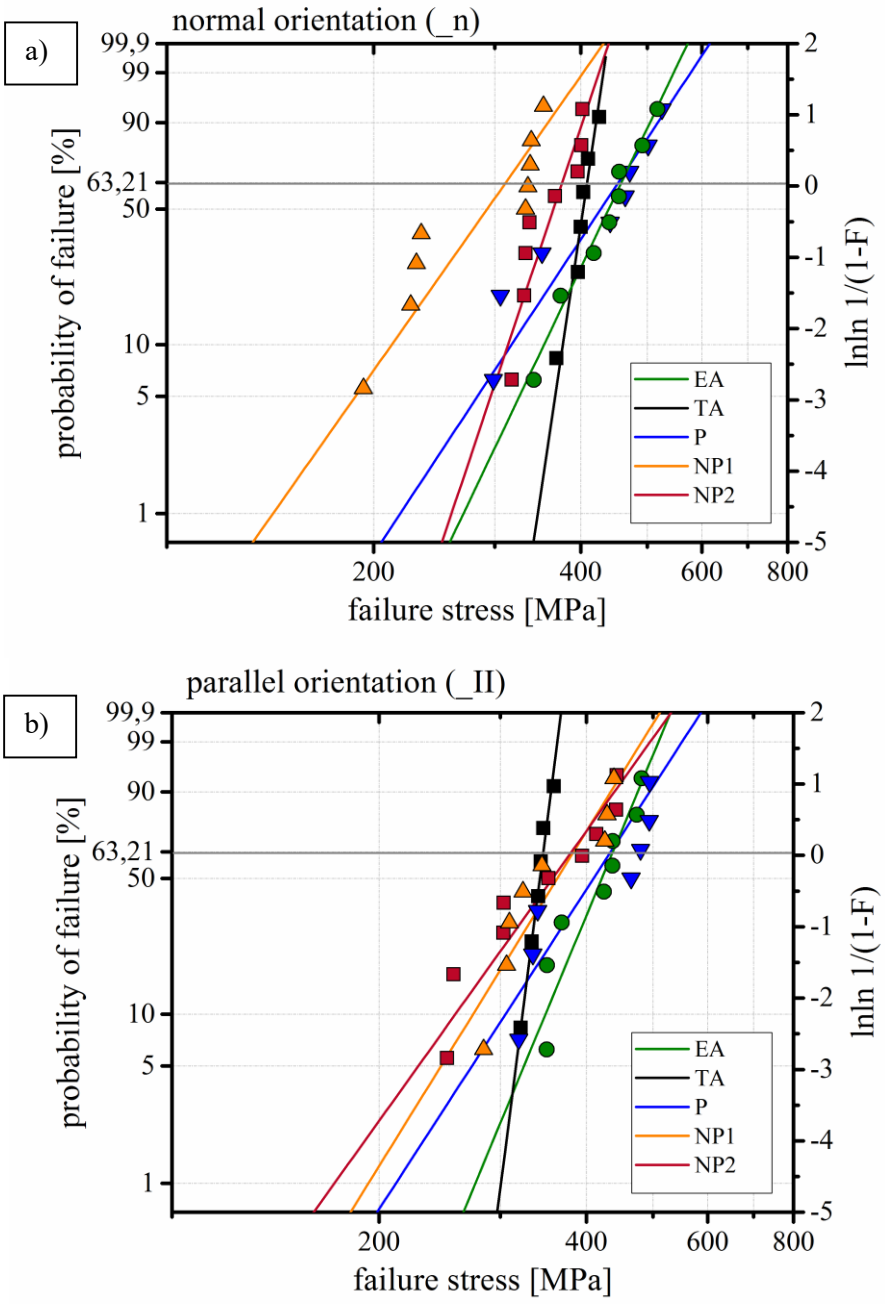

Figure 37. Weibull distribution of chamfered samples tested **a)** perpendicular (_n) and **b)** parallel (_II) to the layers

In consideration of the collected and evaluated data the different designs of monoliths and laminates provided similar values according to the corrected bending strength and the characteristic strength. The strengths for the different designs and testing directions varied from 310 to 410 MPa. The similar results among the different designs were probably caused by similar defects introduced during fabrication. Hence, none of the designs shows significantly different properties in strength.

Additionally, the applied equation (18) for the evaluation of the bending strength considers specimens of a monolithic microstructure, and not laminates. The influence of the different layers in the laminates was not included in the calculations.

4.4.1.1. Fractographic analysis

The fractographic analysis aimed to determine whether certain shapes or positions of defects have an influence on the resulting bending strength. It was distinguished between small cracks at the surface, defects close to the surface and volume defects.

The defects were classified, regarding to the taken SEM pictures from the fractured surfaces, as seen in Figure 38. Table 15 gives an overview on found defects in the samples of different designs (EA, TA, P, NP1, NP2), tested in two different directions (_II and _n) and the correlating measured bending strengths. Further, with this classification of defects estimations for critical crack lengths were made.

Considering the Weibull distributions of the EA, P and NP1 samples (see Figure 37), it was observed that some of the specimens showed similar strengths. Putting the measured strengths with the classified defects in correlation, a trend for the EA and P samples could be observed. Especially the samples with volume defects reached higher strengths than those with a small crack at or close to the surface.

However, for the NP1 samples, this trend could not be proved, it actually occurred vice versa (see Table 15). Here, the similar strengths at two different values (Figure 37) might be due to the different batches, from which the samples were taken. Furthermore, the volume defects determined were a result of weak interfaces between the different layers. This led to defects, which had a one-dimensional shape, as seen in Figure 38j). This observations was also made for samples of the NP2 design, see Table 15.

Another explanation for the correlation of the measured bending strength and the determined defects is the size of the defects. Considering the Figure 38k) – n) it was observed, that large defects (<50 µm) resulted in low strength and vice versa.

Table 15: Overview of the bending strengths of samples of the different designs and the effective defect for failure

sample	disposition of defect	$\sigma_{B,corr}$ [MPa]	sample	disposition of defect	$\sigma_{B,corr}$ [MPa]
EA#3_3_II	Surface	481	NP1.2_10_II	Surface	439
EA#3_2_II	Volume	473	NP1.2_8_II	Surface	429
EA#3_4_II	Close to Surface	437	NP1.3_6_II	Surface	345
EA#5_4_n	Volume	517	NP1.3_2_II	Volume	309
EA#5_6_n	Volume	492	NP1.3_4_II	Volume	283
EA#5_5_n	Close to surface	374	NP1.4_2_n	Close to surface	353
TA#2_7_II	Surface	347	NP1.4_7_n	Surface	339
TA#4_1_II	surface	344	NP1.4_5_n	Surface	338
TA#3_2_II	Surface	321	NP1.3_10_n	Surface	231
TA#4_5_n	Surface	426	NP1.3_7_n	Surface	226
P#3_7_II	Volume	494	NP1.3_8_n	Surface	193
P#3_2_II	Close to surface	494	NP2.3_4_II	Volume	443
P#3_6_II	Volume	465	NP2.3_2_II	Surface	394
P#3_5_II	Close to surface	334	NP2.3_3_II	Surface	353
P#3_4_II	Close to surface	319	NP2.4_2_II	Volume	304
P#4_6_n	Volume	525	NP2.4_1_II	Volume	303
P#4_3_n	Surface	464	NP2.5_3_n	Close to surface	402
P#4_4_n	Surface	306	NP2.6_1_n	Surface	401
P#4_2_n	Close to surface	299	NP2.5_2_n	Surface	396
			NP2.6_3_n	Surface	331
			NP2.5_1_n	Surface	318

Considering all the different influences of defects on the resulting strength of the different materials and designs, it can be said that due to the processing a number of defects of different kind and location was introduced during the fabrication. These defects were identified as failure origin for all samples.

In future work, the processing must be optimized, in order to fabricate samples with a lower amount of defects and a higher consistency of the microstructure among the single batches.

a) EA#3_3_II [481 MPa]

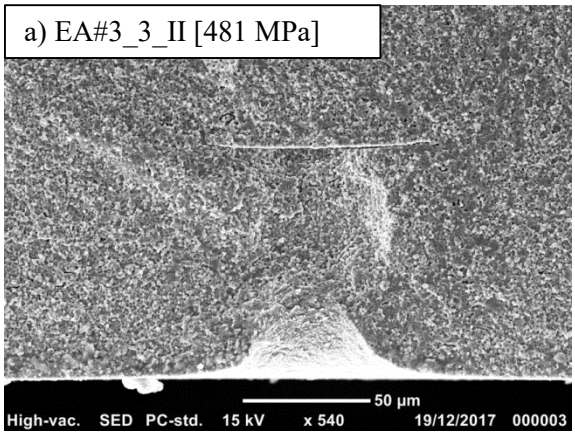

b) EA#3_2_II [474 MPa]

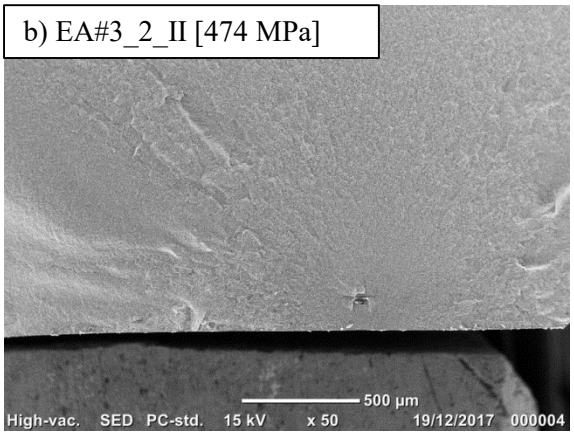

c) EA#5_4_n [517 MPa]

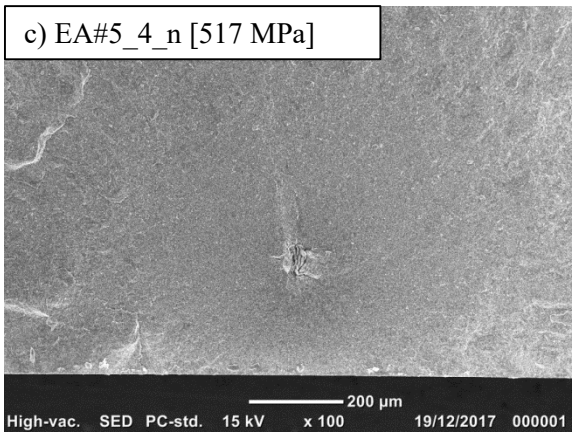

d) EA#5_5_n [374 MPa]

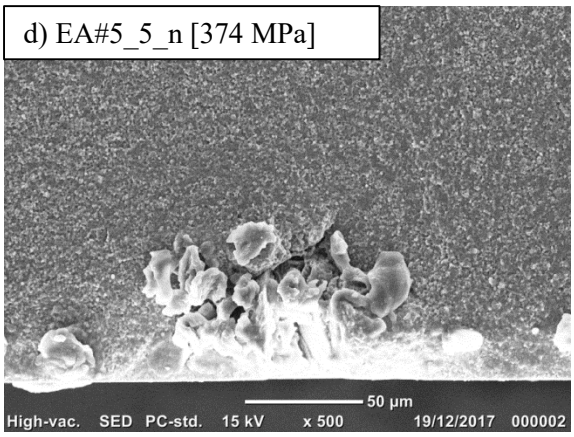

e) TA#2_7_II [347 MPa]

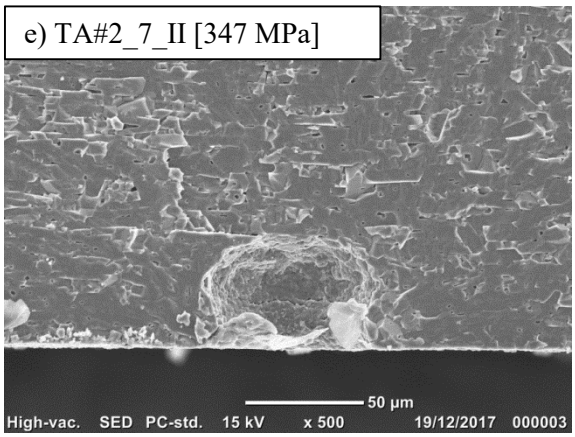

f) TA#4_5_n [425 MPa]

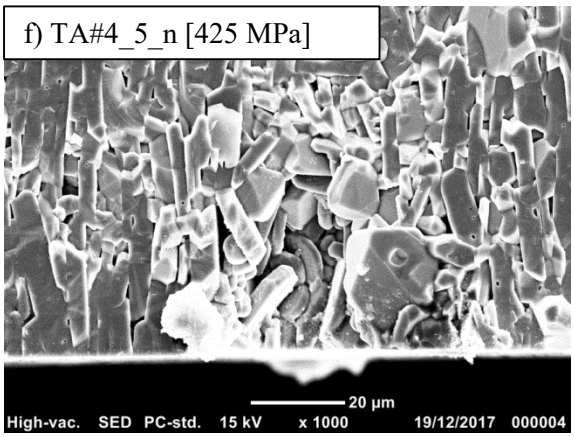

g) P#3_2_II [494 MPa]

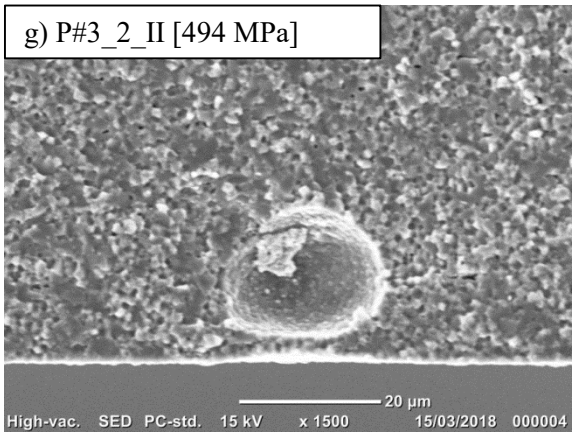

h) P#3_5_II [334 MPa]

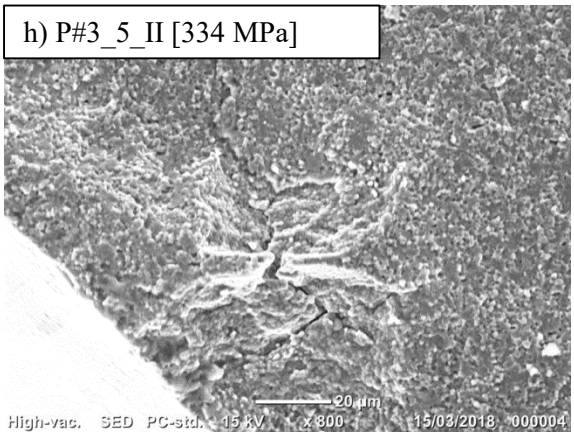

i) P#4_6_n [525 MPa]

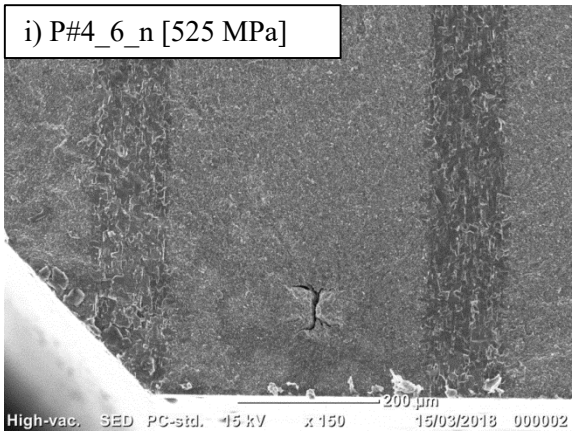

j) P#4_4_n [306 MPa]

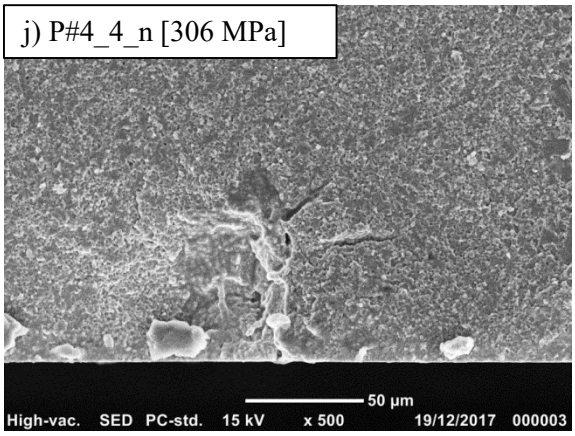

k) NP1.2_10_II [438 MPa]

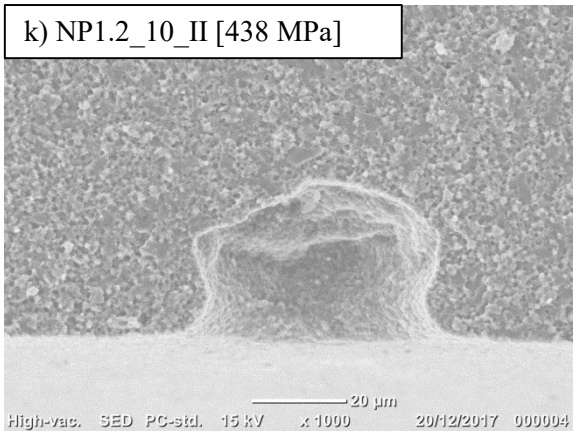

l) NP1.3_2_II [309 MPa]

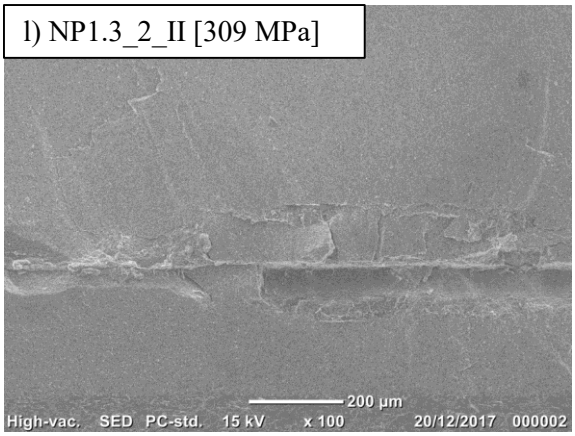

m) NP1.4_2_n [353 MPa]

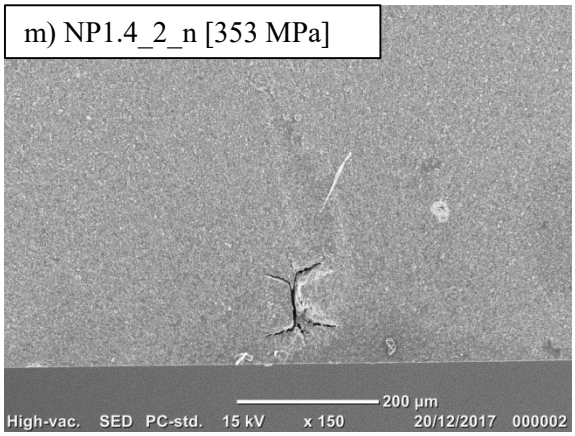

n) NP1.3_8_n [193 MPa]

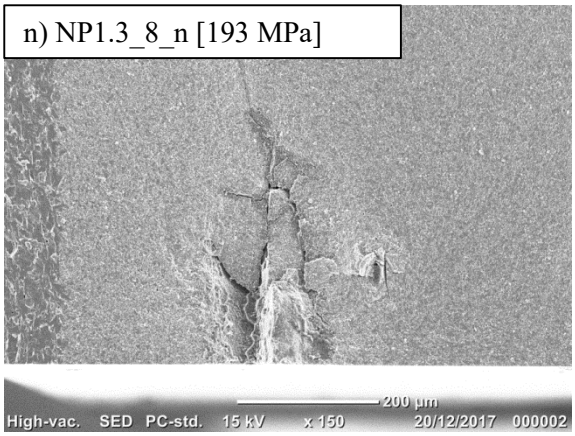

o) NP2.3_4_II [443 MPa]

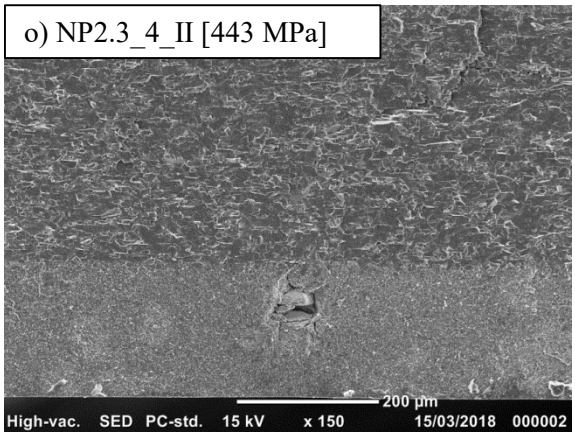

p) NP2.3_3_II [353 MPa]

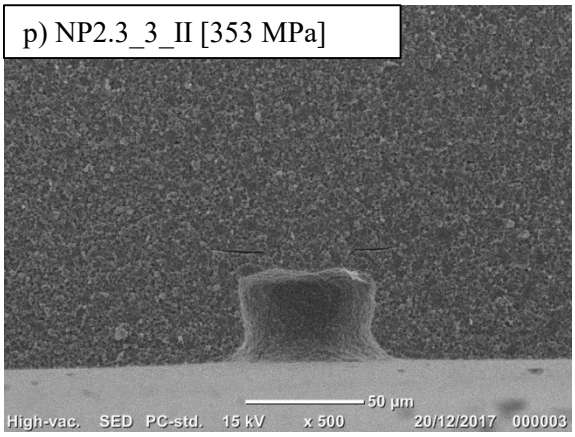

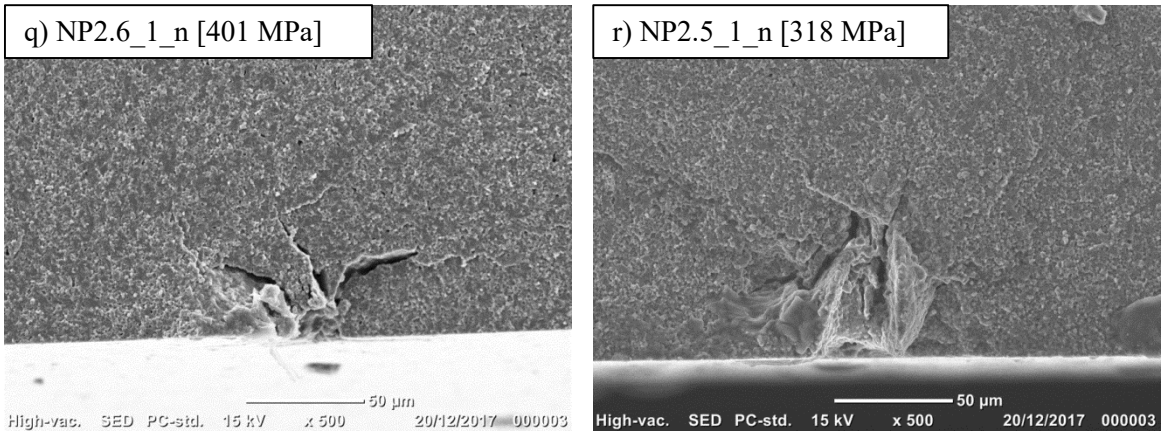

Figure 38. a) to **r)** show defects in the microstructure of selected samples of the different designs (EA, TA, P, NP1, NP2) tested in two directions (_II & _n)-textured microstructure pictured with a SEM

According to the observed fracture surfaces, volume defects as well as surface defects were found in all the different designs (EA, TA, P, NP1 and NP2). The critical crack length was estimated according to the Griffith criterion:

$$a_c = \frac{1}{\pi}\left(\frac{K_{1C}}{(\sigma_{max}-\sigma_{res})\cdot Y}\right)^2 \quad (26)$$

where a_c is the critical crack length in [m], K_{IC} is the fracture toughness in [MPam$^{1/2}$], σ_{max} is the maximum corrected bending strength in [MPa], σ_{res} are the residual tensile stresses occurring in the outermost layers of the laminates and Y the non-dimensional geometrical factor of the crack shape. For the calculation of the equiaxed and laminated designs the K_{IC} value of the equiaxed alumina was employed, whereas for the textured design the K_{IC} of textured alumina was used.

In Table 16 the different crack shapes are classified and the correlating geometrical factors are listed [58].

Table 16: Geometrical factors depending on shape of the defects [58]

Geometrical factor		
Y_1	Small surface cracks	0.73
Y_2	Defects close to surface	$\frac{2}{\pi}\sqrt{2}$
Y_3	Volume defects away from the surface	$\frac{2}{\pi}$

Table 17 summarizes the calculated critical crack lengths, depending on the different geometrical factors and the maximum bending strength.

Table 17: Data of the critical crack length, according to the different geometrical factors

	F_{max}	σ_{max}	a_{c1}	a_{c2}	a_{c3}
	[N]	[MPa]	[µm]	[µm]	[µm]
EA_n	600 ±92	392 ±58	58.7 ±19.4	38.6 ±12.7	77.1 ±25.5
EA_II	538 ±74	370 ±53	65.1 ±19.2	42.8 ±12.6	85.6 ±25.2
TA_n	578 ±40	363 ±26	64.9 ±9.1	42.7 ±6.0	85.3 ±12.0
TA_II	413 ±27	296 ±13	97.0 ±8.5	63.8 ±5.6	127.5 ±11.1
P_n	303 ±61	366 ±87	73.9 ±36.8	48.6 ±24.2	97.2 ±48.4
P_II	257 ±48	387 ±75	63.5 ±28.5	41.7 ±18.7	83.5 ±37.5
NP1_n	249 ±59	250 ±65	169.1 ±104.0	111.1 ±68.4	222.3 ±136.8
NP1_II	241 ±41	307 ±66	102.2 ±44.8	67.2 ±29.5	134.4 ±58.9
NP2_n	847 ±91	316 ±35	87.5 ±19.1	57.5 ±12.6	115.1 ±25.1
NP2_II	741 ±150	326 ±76	107.5 ±56.3	70.7 ±37.0	141.3 ±74.0

Most of the defects as shown in the SEM images of the fracture surfaces had a size of about 50 µm. Comparing the measurements with the calculated critical values, it was observed that when considering the geometric factor for defects close to the surface (Y_2) the critical crack length corresponds to the actual size of the defects (~50 µm). However, the critical value for small surface cracks (Y_1) and volume defects away from the surface (Y_3) are bigger than the examined natural defects in the sample. In order to understand the interaction of propagating cracks with the different layered architectures, indentation-strength test were performed.

4.4.2. Indentation Strength of monoliths and laminates

The purpose of testing the indentation strength was to determine the effects of crack arrest, bifurcation and deflection. The inserted artificial flaws were the effective defects, causing the samples to fail. The use of different loads yielded artificial flaws with different sizes, here categorized as (i) large (10 kg), (ii) middle (5 kg) and (iii) small (2 kg). The laminate samples were tested (i) perpendicular (_n) and (ii) parallel (_II) to the layers. Figure 39a) and b) show the strengths of the different designs, (i) equiaxed alumina (EA), (ii) textured alumina (TA), (iii) periodic design (P), (iv) non-periodic design 1 (NP1) and (v) non-periodic design 2 (NP2) of the different testing directions as a function of the crosshead displacement. The strength

was evaluated according to the equation (18), as described in 4.4.1. Additionally to Figure 39, in Table 18 the maximum force and the resulting maximum strength for the specimen, showing the highest resistance, for each design and testing direction is listed. Further, the average force and strength of all tested specimen of each design is displayed. It can be observed that the highest strengths were achieved with the non-periodic design 1 and 2, where the force was applied parallel to the layers, as also clearly displayed in Figure 39.

Table 18: List of maximum and average force and the resulting strength

	Maximum force (F_{max})	Average force (F)	Maximum strength (σ_{max})	Average strength (σ)
	[N]	[N]	[MPa]	[MPa]
EA_n	223	219 ±26	150	149 ±2
EA_II	223	208 ±13	174	163 ±11
TA_n	348	318 ±45	255	231 ±31
TA_II	271	256 ±16	225	210 ±15
P_n	141	137 ±8	176	175 ±7
P_II	105	96 ±10	159	150 ±8
NP1_n	115	100 ±14	138	135 ±2
NP1_II	214	186 ±26	304	289 ±14
NP2_n	327	305 ±25	131	123 ±8
NP2_II	620	575 ±45	273	251 ±20

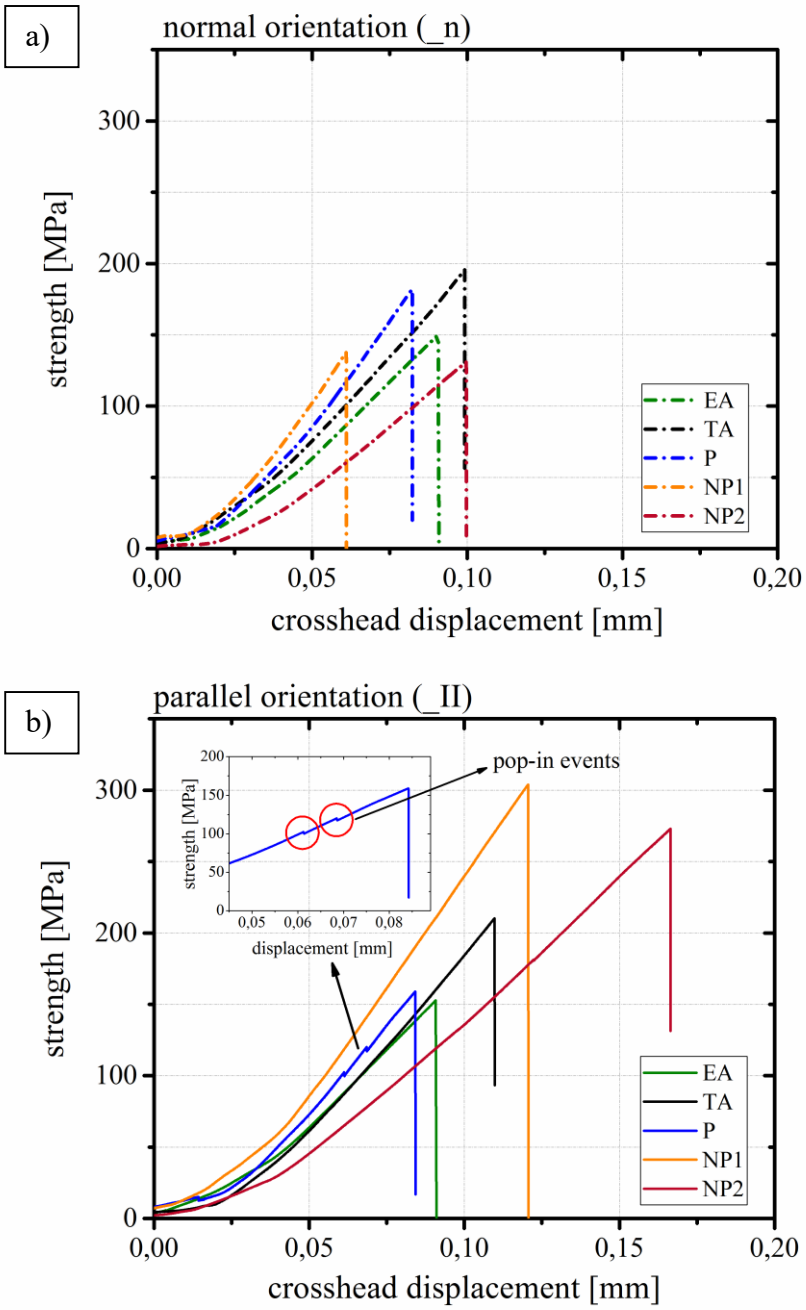

Figure 39. a) shows the representative curves, where the testing direction was perpendicular (_n) to the layers of the samples and **b)** displays the curves of the parallel (_II) orientation

At the perpendicular testing direction, the strengths of the different designs were in the range of 100 to 200 MPa. In comparison it was remarkable that in the parallel direction, the non-periodic designs 1 and 2 achieved strength values at least 50 MPa higher than the other designs. This validates the hypothesis that the non-periodic disposition of the compressive layers might enhance the fracture resistance of the ceramic design. The combination of

compressive stress and relatively thick compressive layers favored crack arrest from different indents, and promoted crack deflection and bifurcation of the propagating crack.

Additionally, it was observed that “pop-ins” occurred at the tested laminated samples. The first “pop-in” occurred at the 10 kg indent, where crack arrest happened. The next pop-in corresponded to the middle size indent (5 kg), and the smallest indent (2 kg) was the critical flaw, which finally led to failure. This behavior could be clearly observed at 2 out of 5 samples for the periodic design and at 4 out of 5 for the non-periodic design 2, see Table 19.

Table 19: List of tested samples breaking at a certain indent

Design	Total number of tested samples	Number of samples, failing at the indent of a certain load (2, 5, 10 kg)		
		2 kg	5 kg	10 kg
EA_n	2			2
EA_II	4			4
TA_n	3			3
TA_II	3			3
P_n	3			3
P_II	5	2	3	
NP1_n	5			5
NP1_II	5		2	3
NP2_n	5			5
NP2_II	5	4	1	

4.4.2.1. Fractographic analysis

In the fractographic analysis the polished side surfaces were analyzed after failure, to display the effects of crack arrest and deflection. Scanning electron microscope (SEM) as well as optical light microscope (LIMI) were employed. Figure 40a) and b) display the crack leading to failure in a periodic sample, showing the effects of crack deflection and bifurcation. The effective artificial flaw in this sample that led to failure was the indent of a 5 kg load. Figure 40c) and d) show the arrested crack at the indent of 10 kg. Figure 40e) and f) show another example of the periodic design where crack arrest occurred at the 10 kg indent, resulting in a “pop-in” in the stress-displacement curve.

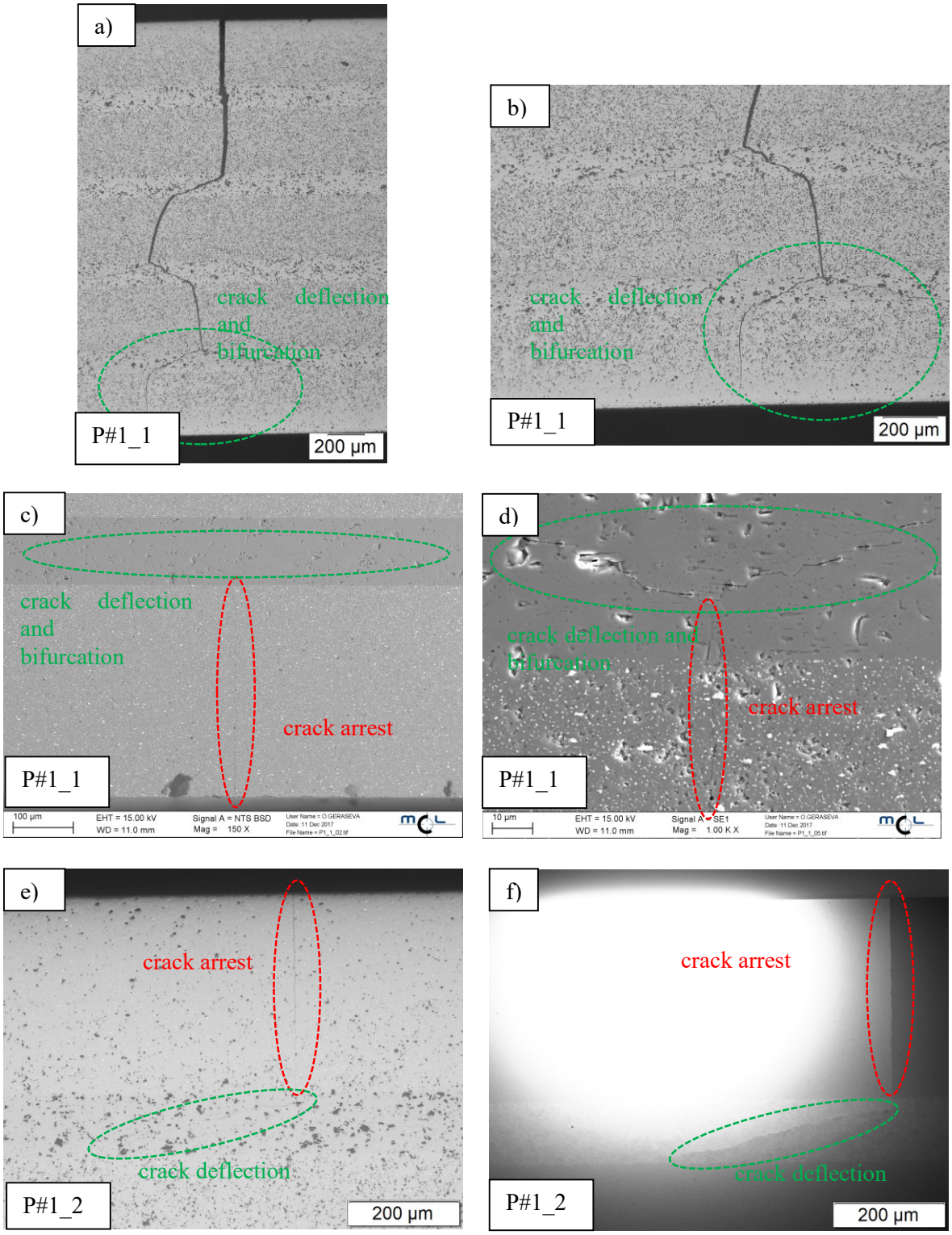

Figure 40. Pictures **a)** to **f)** show representative samples of the periodic design showing the effects of crack arrest, deflection and bifurcation taken with the SEM and LIMI.

For comparison, Figure 41 shows some representative fractures of the non-periodic design (NP). For the non-periodic designs 1 and 2 the effects of crack arrest at the indents of 5 and 10 kg was also observed, especially on NP2 samples. Figure 41a) shows the crack, which lead

to failure at the 2 kg indent, and its deflection in the textured layers, on the polished side surface of an NP2 sample. Figure 41b) and d) show the effect of crack arrest at the 5 kg indent on a NP2 specimen, in two different magnifications. Figure 41d) and e) show the same sample, at two different positions where crack arrest occurred (i.e. from the 5kg and 10kg indent, respectively).

According to the fractographic analysis of the non-periodic designs, it could be observed that a higher number of samples showed crack arrest at the 5 and 10 kg indent, as compared to the periodic design. This could not be clearly determined with only the bending strength, where the “pop-ins” of the curves were not as significant for the non-periodic designs as it was observed for the periodic designs.

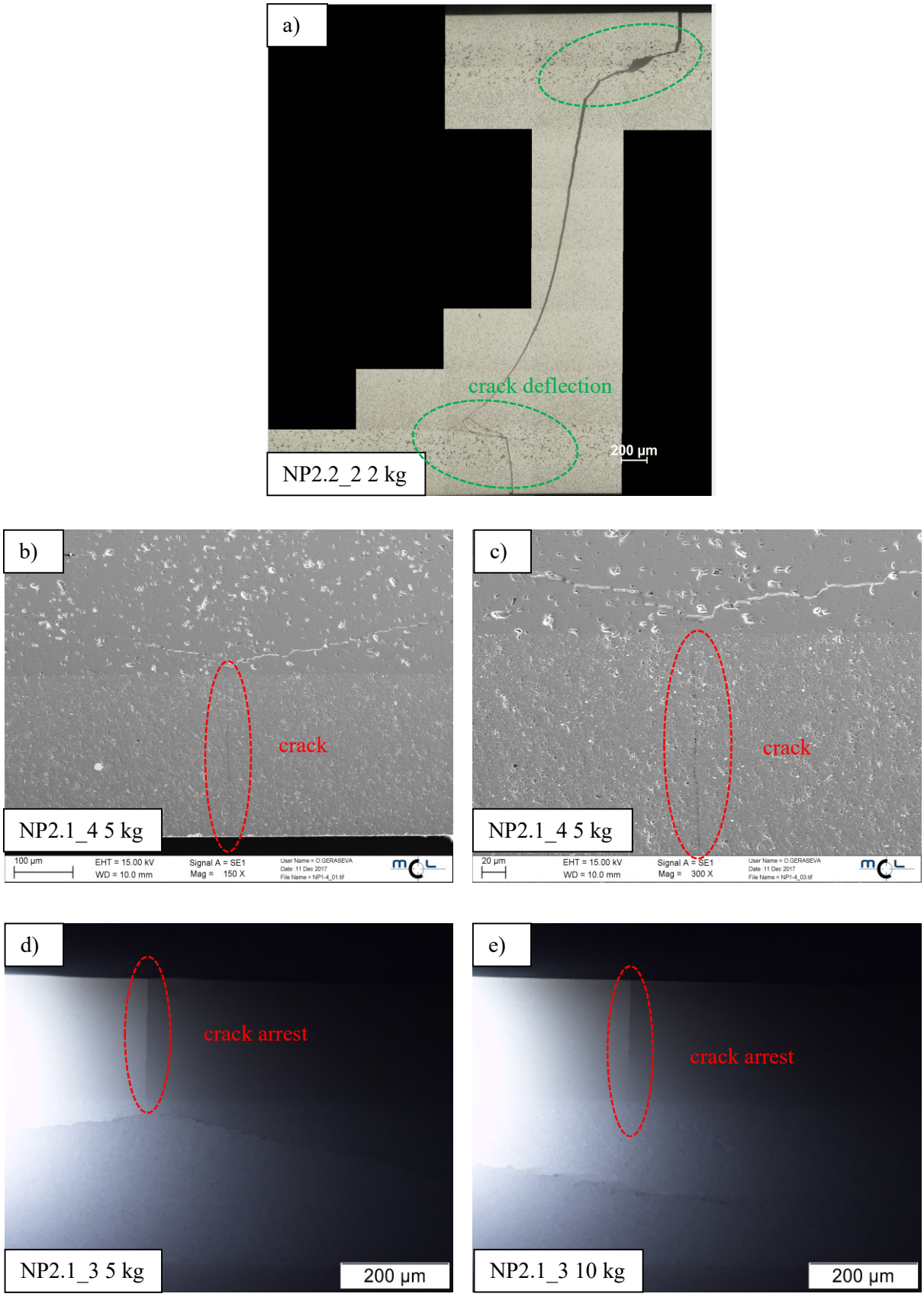

Figure 41. These variety of SEM- and LIMI-pictures shows representative samples of the non-periodic design 2, showing the propagation of the critical crack in **a)**; and **b)** to **e)** show crack arrests at certain sizes of indents (5 and 10 kg).

5. Summary and conclusion

In this thesis the design, processing and characterization of alumina-based layered structures was carried out.

Monolithic materials of different microstructures, (i) equiaxed alumina (EA) and (ii) textured alumina (TA), were fabricated via tape casting. The monolithic samples of EA and TA were further characterized regarding to their microstructural, thermo-physical and mechanical properties.

Considering the microstructural characterization, SEM-pictures and X-Ray diffraction was made, to determine the degree of texture with the Lotgering factor (LF), especially for the textured alumina. For the fabricated textured alumina LFs from 41 to max. 71 %vol were achieved, which is comparably low to the desired value of <90 %.

Further, thermal, physical and mechanical properties as density, hardness, E-modulus, coefficient of thermal expansion and fracture toughness were determined.

The bulk densities of the equiaxed and textured material were measured according to the Archimedes principle. The resulting relative density (ρ_{rel}) of the equiaxed alumina was about 99 %, in comparison to the textured alumina having 96 %.

For the evaluation of the hardness a Vickers indenter was utilized, applying loads of 2, 5, 10 and 20 kg. The values of Vickers hardness were for the EA material between 2175 and 1815, and for the TA material between 1545 and 1410, both showing a decrease of hardness with increasing applied load.

The Young's-modulus for both monolithic materials (EA and TA) was approximately 380 GPa, being in the same range as the theoretical E-modulus (= 380-405 GPa) [3,9,48]
As a thermal property, the coefficient of thermal expansion (*CTE*) was determined via dilatometry. The resulting *CTE* for the equiaxed monolith was about 8.2 E-06 K^{-1} and for the textured monolith about 7.8 E-06 K^{-1}. The higher *CTE* of EA, is due to the added zirconia, which shows a higher thermal expansion than alumina.

Finally, the fracture toughness (K_{IC}) was evaluated after the SEVNB method. Comparing the values for K_{IC} for the equiaxed ($K_{IC,\ EA}$ = 3.8 $MPam^{1/2}$) and textured alumina ($K_{IC,\ TA}$=4.4 $MPam^{1/2}$), it is observed that TA shows higher fracture toughness. This is a result of the oriented microstructure, where the cracks are deflected intergranularly parallel to the surface on which the load is applied. As a result, the distance

that has to be covered by the crack causing failure increases, leading to a necessity of a higher applied stress (σ [MPa]).

Additionally, to the monolithic samples, laminated samples of three different architectures (i) periodic design (P), non-periodic design 1 (NP1) and non-periodic design 2 (NP2) were fabricated. These laminates were composites of layers of equiaxed and textured alumina. Due to the different CTEs of these two materials, residual tensile stresses were induced in the EA layers and residual compressive stresses were generated in the TA layers. The induced residual stresses in the different layers were $\sigma_{res, EA}$ = 45 MPa, and $\sigma_{res, TA}$ = -270 MPa for all designs.

The aim was to determine the effects of crack arrest, crack deflection and crack bifurcation as a result of especially the induced residual compressive stresses. For the evaluation strength tests were performed with (i) natural and (ii) artificial flaws, the latter made with a Vickers indenter. Additionally, to the laminates, also the monolithic materials EA and TA were tested for comparison.

The evaluation of the strength and indentation strength was accomplished via 4-Point-Bending testing. Samples of the five different architectures (i) equiaxed alumina (EA), (ii) textured alumina (TA), (iii) periodic design (P), (iv) non-periodic design 1 (NP1) and (v) non-periodic design 2 (NP2) were tested in two different directions (a) perpendicular and (b) parallel to the layers.

The measured bending strength of the samples with natural flaws were plotted in a Weibull diagram. Considering the Weibull distribution of the bending strength, it was observed that the characteristic strengths of the five architectures and both testing directions are in a range of approximately 300-500 MPa.

Further, when observing the curves of strength [MPa] as a function of the crosshead displacement [mm], it was seen that for the tests performed perpendicular to the layers, the equiaxed material achieved the highest strength (σ_B~480 MPa), whereas the bending strengths of the other architectures (TA, P, NP1 and NP2) range from about 310 to 400 MPa.

In contrast, considering the measurements of the samples tested parallel to the layers, it was found that the bending strengths of the laminates achieved results comparable to the strength value of equiaxed alumina. The values of the EA, P, NP1 and NP2 design are from approximately 410 to 470 MPa. Only the textured alumina achieved a lower value of σ_B~320 MPa.

The fractography of these tested samples showed that there were a high number of different defects in the material. Surface defects as well as volume defects close to and below the surface were found.

For the evaluation of the indentation strength, artificial flaws of three different loads (2, 5 and 10 kg) were induced. The tests were performed in the two directions, perpendicular and parallel to the layers, always inducing the indents on the surface potentially under tension. Considering the measured indentation strengths of the samples tested perpendicular to the layers, the textured and the periodic designs achieved the highest values (σ=160-200 MPa). In comparison, EA, NP1 and NP2 reached indention strengths of 140 to 150 MPa. When testing parallel to the layers,

the non-periodic designs 1 and 2 showed the highest values (σ=275-300 MPa). The other designs (TA, EA and P) achieved indention strengths in a range of approximately 150 to 210 MPa.

According to the pop-ins in the strength curves and the fractography, in several examined laminates of the different designs (P, NP1 and NP2), the effects of crack arrest, crack deflection and crack bifurcation due to induced residual stresses and the combined microstructures, were observed. This was associated with the combined effect of architecture and residual stress in the layers.

Although, fracture toughness could be improved through textured microstructures and effects such as crack arrest, deflection and bifurcation could be observed, some desired improvements as higher strengths due to residual stresses in laminated compounds could not be achieved. A reason of not being able to fulfill all the desired aims might have been the high number of present defects in the microstructure due to processing, leading to the conclusion that the processing has to be refined to achieve specimens of higher mechanical properties.

References

[1] B. Derjaguin, “A theory of interaction of particles in presence of electric double layers and the stability of lyophobe colloids and disperse systems,” *Progress in Surface Science*, vol. 43, 1-4, pp. 1–14, 1993.

[2] M. F. Ashby and D. R. Jones, “The mechanical properties of ceramics,” in *Engineering Materials*: *An Introduction to Microstructures, Processing and Design,* Michael F. Ashby, David R.H. Jones, Ed., pp. 177–184, Elsevier, 1998.

[3] R. Danzer, T. Lube, R. Morrell et al., “Mechanical Properties of Ceramics,” in *Handbook of Advanced Ceramics*, pp. 609–632, Elsevier, 2013.

[4] R. Bermejo, “Structural Integrity of Alumina - Zirconia Multilayered Ceramics: Doctoral Thesis, Univeristat Politecnica de Catalunya,” 2006.

[5] B. Derjaguin and L. Landau, “Theory of the stability of strongly charged lyophobic sols and of the adhesion of strongly charged particles in solutions of electrolytes,” *Progress in Surface Science*, vol. 43, 1-4, pp. 30–59, 1993.

[6] M. B. G. Trefalt, “Overview of DLVO Theory,” 2014.

[7] M. N. Rahaman, *Sintering of Ceramics*, Taylor and Francis, Hoboken, 2007.

[8] W. D. Kingery, H. K. Bowen, and D. R. Uhlmann, *Introduction to ceramics*, Wiley, New York, 1976.

[9] P. Auerkari, *Mechanical and physical properties of engineering alumina ceramics*, Technical Research Centre of Finland, Espoo, 1996.

[10] Michael F. Ashby, David R.H. Jones, ed., *Engineering Materials*: *An Introduction to Microstructures, Processing and Design*, Elsevier, 1998.

[11] R. Danzer, T. Lube, P. SUPANCIC et al., “Fracture of Ceramics,” *Advanced Engineering Materials*, vol. 10, no. 4, pp. 275–298, 2008.

[12] M. E. NORDBERG, E. L. MOCHEL, H. M. GARFINKEL et al., “Strengthening by Ion Exchange,” *Journal of the American Ceramic Society*, vol. 47, no. 5, pp. 215–219, 1964.

[13] Sylvian Deville, Eduardo Saiz, Ravi K. Nalla, and Antoni P.Tomsia, “Freezing as a Path to Build Complex Composites,” *Science,* no. 311, pp. 515–518, 2006.

[14] G. L. Messing, S. Poterala, Y. Chang et al., “Texture-engineered ceramics—Property enhancements through crystallographic tailoring,” *Journal of Materials Research*, vol. 32, no. 17, pp. 3219–3241, 2017.

[15] Y. Chang, R. Bermejo, G. L. Messing et al., “Improved Fracture Behavior of Alumina Microstructural Composites with Highly Textured Compressive Layers,” *Journal of the American Ceramic Society*, vol. 97, no. 11, pp. 3643–3651, 2014.

[16] Y. Chang, R. Bermejo, O. Ševeček et al., “Design of alumina-zirconia composites with spatially tailored strength and toughness,” *Journal of the European Ceramic Society*, vol. 35, no. 2, pp. 631–640, 2015.

[17] A.Goyal, R. Feenstra, F.A. List, M. Paranthaman, D.F. Lee, D.M. Kroeger, D.B. Beach, J.S. Morell, T.G. Chirayil, D.T. Verebelyi, X. Cui, E.D. Specht, D.K. Christen, and P.M. Martin, “Using RABiTS to fabricate high-temperature superconducting wire,” *The Journal of Minerals, Metals & Materials Society,* no. 51, pp. 19–23, 1999.

[18] S. Jin, R. C. Sherwood, R. B. van Dover et al., “High TC superconductors—composite wire fabrication,” *Applied Physics Letters*, vol. 51, no. 3, pp. 203–204, 1987.

[19] G. L. Messing, S. Trolier-McKinstry, E. M. Sabolsky et al., “Templated Grain Growth of Textured Piezoelectric Ceramics,” *Critical Reviews in Solid State and Materials Sciences*, vol. 29, no. 2, pp. 45–96, 2004.

[20] H. Yilmaz, G.L. Messing, S. Trolier-McKinstry, “(Reactive) Templated Grain Growth of Textured Sodium Bismuth Titanate,” *Journal of Electroceramics,* no. 11, pp. 207–215, 2003.

[21] Y. SAKKA and T. S. SUZUKI, “Textured Development of Feeble Magnetic Ceramics by Colloidal Processing Under High Magnetic Field,” *Journal of the Ceramic Society of Japan*, vol. 113, no. 1313, pp. 26–36, 2005.

[22] R. J. Pavlacka and G. L. Messing, “Processing and mechanical response of highly textured Al2O3,” *Journal of the European Ceramic Society*, vol. 30, no. 14, pp. 2917–2925, 2010.

[23] G. Gottstein, *Materialwissenschaft und Werkstofftechnik*: *Physikalische Grundlagen*, Springer Vieweg, Berlin, 2014.

[24] F.K. Lotgering, “Topotactical reactions with ferrimagnetic oxides having hexagonal crystal structures—I,” *J. Inorg. Nucl. Chem.,* no. 9, p. 113, 1959.

[25] I. J. MacColm, *Ceramic hardness*, Plenum Pr, New York u.a., 1990.

[26] T. Carisey, I. Levin & D.G. Brandon, “Microstructure and Mechanical Properties of Textured Al2O3,” *Journal of the European Ceramic Society,* no. 15, p. 283, 1995.

[27] V. R. Vedula, S. J. Glass, D. M. Saylor et al., “Residual-Stress Predictions in Polycrystalline Alumina,” *Journal of the American Ceramic Society*, vol. 84, no. 12, pp. 2947–2954, 2001.

[28] B. Lawn, *Fracture of brittle solids*, Cambridge University Press, Cambridge, 1993.

[29] R. Pavlacka, R. Bermejo, Y. Chang et al., “Fracture Behavior of Layered Alumina Microstructural Composites with Highly Textured Layers,” *Journal of the American Ceramic Society*, vol. 96, no. 5, pp. 1577–1585, 2013.

[30] L. Sestakova, R. Bermejo, Z. Chlup et al., “Strategies for fracture toughness, strength and reliability optimisation of ceramic-ceramic laminates,” *International Journal of Materials Research*, vol. 102, no. 6, pp. 613–626, 2011.

[31] M. Y. He, A. G. Evans, and J. W. Hutchinson, “Crack deflection at an interface between dissimilar elastic materials: Role of residual stresses,” *International Journal of Solids and Structures*, vol. 31, no. 24, pp. 3443–3455, 1994.

[32] E. Dörre and H. Hübner, *Alumina*: *Processing, properties, and applications*, Springer, Berlin, 1984.

[33] “http://tikalon.com/blog/2015/Al2O3.png,” 6/18/2018.

[34] H. Salmang, H. Scholze, and R. Telle, *Keramik*, Springer-Verlag Berlin Heidelberg, Berlin, Heidelberg, 2007.

[35] H. B. S. Terahsima, “Grain Growth: Zener Pinning of Grain Boundaries by Oxide Particles,” 2005.

[36] K. OKADA and T. SAKUMA, “The Role of Zener's Pinning Effect on the Grain Growth in Al2O3-ZrO2,” *Journal of the Ceramic Society of Japan*, vol. 100, no. 1160, pp. 382–386, 1992.

[37] F.F.Lange, “Powder Processing Science and Technology for Increased Reliability,” *Journal of the American Ceramic Society,* no. 72, pp. 3–15, 1989.

[38] “ISO/FDIS 23146:2008, Fine ceramics (advanced ceramics, advanced technical ceramics) - Test methods for fracture toughness of monolithic ceramics - Single-edge V-notch beam (SEVNB) method,”.

[39] T. Nishida, Y. Hanaki, and G. Pezzotti, “Effect of Notch-Root Radius on the Fracture Toughness of a Fine-Grained Alumina,” *Journal of the American Ceramic Society*, vol. 77, no. 2, pp. 606–608, 1994.

[40] “EN 843-1:1995, Hochleistungskeramik, Monolithische Keramik, Mechanische Eigenschaften bei Raumtemperatur, Teil 1: Bestimmung der Biegefestigkeit,”.

[41] W. Walcher, *Praktikum der Physik*, Vieweg+Teubner Verlag, Wiesbaden, 1994.

[42] “EN 843-4:1994, Hochleistungskeramik, Monolithische Keramik, Mechanische Eigenschaften bei Raumtemperatur, Teil 4: Vickers-, Knopp- und Rockwell-Härteprüfung,”.

[43] R. M. German, P. Suri, and S. J. Park, “Review: Liquid phase sintering,” *Journal of Materials Science*, vol. 44, no. 1, pp. 1–39, 2009.

[44] “https://www.tosoh.com/our-products/advanced-materials/zirconia-powders,” 4/5/2018.

[45] Schubert, Reinert, Egberts, Dyck, “Labor für Werkstofftechnik-Fachbereich Maschinenbau,” Hochschule Bremen-Univeristy of Applied Sience.

[46] G. Q. J.B. Quinn, “Indentation brittleness of ceramics: a fresh approach,” *Journal of Materials Science,* no. 32, pp. 4331–4346, 1997.

[47] *Handbook of Advanced Ceramics*, Elsevier, 2013.

[48] K.S. Ravichandran, “Elastic Properties of Two-Phase Composites,” *Journal of the American Ceramic Society,* no. 77, pp. 1178–1184, 1994.

[49] H. Salmang, H. Scholze, and R. Telle, eds., *Keramik*, Springer, Berlin, 2007.

[50] J. A. Salem, J. L. Shannon, and R. C. Brad, “Crack Growth Resistance of Textured Alumina,” *Journal of the American Ceramic Society*, vol. 72, no. 1, pp. 20–27, 1989.

[51] V. M. Sglavo and M. Bertoldi, “Design and production of ceramic laminates with high mechanical reliability,” *Composites Part B: Engineering*, vol. 37, no. 6, pp. 481–489, 2006.

[52] V. M. Sglavo, M. Paternoster, and M. Bertoldi, “Tailored Residual Stresses in High Reliability Alumina-Mullite Ceramic Laminates,” *Journal of the American Ceramic Society*, vol. 88, no. 10, pp. 2826–2832, 2005.

[53] O. Sevecek, M. Kotoul, D. Leguillon, E. Martin, R. Bermejo, “Understanding the edge crack phenomenon in ceramic laminates,” *Frattura ed Integrita Strutturale,* no. 34, pp. 408–416, 2015.

[54] O. Ševeček, M. Kotoul, D. Leguillon et al., “Modelling of edge crack formation and propagation in ceramic laminates using the stress–energy coupled criterion,” *Engineering Fracture Mechanics*, vol. 167, pp. 45–55, 2016.

[55] F.I. Baratta, W.T. Matthews, G.D. Quinn, “Errors Associated with flexure Testing of brittle materials,” *U.S. Army Materials Technology Laboratory*, 1987.

[56] “EN-843-5:1996, Advanced technical ceramics, Monolithic ceramics, Mechanical tests at room temperature, Part 5: Statistical analysis,”.

[57] W. Weibull, “Statistical Theory of Strength of Materials,” *Proc Royal Swedish Inst Eng Res,* no. 151, pp. 1–45, 1939.

[58] R. Danzer, “On the relationship between ceramic strength and the requirements for mechanical design,” *Journal of the European Ceramic Society*, vol. 34, no. 15, pp. 3435–3460, 2014.

List of Tables

List of Figures